Journal of Alloys and Compounds 975 (2024) 172929

Contents lists available at ScienceDirect

Journal of Alloys and Compounds

journal homepage: www.elsevier.com/locate/jalcom

Research article

# Effect of γ forming element additions on the homogenization behavior and formation of hierarchical microstructures in Ni-based superalloys

Mingshuai Huang [a,1], Yiqin Ma [a,1], Yuan Wu [b], Weiwei Zheng [b], Michael J. Pavel [c], Mark L. Weaver [c], Wenxing Meng [d,e], Yan Long [d,e], Sieglind Ngai [f,g,h], Xiaojian Wang [a], Peng Zhang [a], Wei Li [a,*], Florian Vogel [f,g,h,**]

[a] Jinan University, Institute of Advanced Wear & Corrosion Resistant and Functional Materials, Guangzhou 510632, Guangdong, China
[b] University of Science and Technology Beijing, State Key Laboratory for Advanced Metals and Materials Beijing, Beijing 100083, China
[c] Department of Metallurgical and Materials Engineering, The University of Alabama, Tuscaloosa, AL 35401-0202, USA
[d] Guangdong Provincial Key Laboratory for Processing and Forming of Advanced Metallic Materials, Guangzhou 510640, Guangdong, China
[e] School of Mechanical and Automobile Engineering, South China University of Technology, Guangzhou 510640, Guangdong, China
[f] Pico Electron Microscopy Center, Innovation Institute for Ocean Materials Characterization Technology, Center for Advanced Studies in Precision Instruments, Hainan University, Haikou 570228, Hainan, China
[g] Key Laboratory of Pico Electron Microscopy of Hainan Province, Hainan University, Haikou 570228, Hainan, China
[h] School of Materials Science and Engineering, Hainan University, Haikou 570228, Hainan, China

ARTICLE INFO

*Keywords:*
Segregation
Diffusion
Superalloy
Homogenization
Hierarchical microstructure

ABSTRACT

Here, we study the homogenization behavior and microstructure of seven Ni-Al-Ti alloys with quaternary additions of γ forming elements 4Cr, 4Co, 4Ru, 4Mo, 4Hf, 4 W and 2Re. To design a homogenization treatment, the as-cast microstructure is analyzed revealing the diffusion distances *x* between dendrite cores and interdendritic regions. The temperatures for homogenization are determined using differential scanning calorimetry (DSC) and Thermo-Calc simulations, to be between 1150 and 1275 °C. The time to achieve homogenization is modelled based on the residual segregation index δ utilizing diffusion distance, homogenization temperature and diffusion data. Electron probe micro analyzer (EPMA) measurements show that our predictions match for the 4Cr, 4Co, 4Ru, 4 W and 2Re alloys while the 4Hf alloy shows insufficient homogenization. Transmission electron microscopy (TEM) reveals a two-phase γ/γ' microstructure after 750 °C / 24 h, whereby the 4Co and 4Ru alloys form hierarchical microstructures. We observe γ plates in the 4Co alloy and γ spheres in the 4Ru alloy. Ru in the 4Ru alloy is involved in stabilizing the morphology of γ spheres. We provide a straightforward method for the design of homogenization treatments of Ni-based superalloys and demonstrate an alloy design pathway for tailoring the phase stability of hierarchical microstructures.

## 1. Introduction

Ni-based superalloys provide the primary material for key components in extremely hot and corrosive environments. They generally show excellent high-temperature strength, creep and rupture resistance and corrosion resistance. With this unique combination of properties, Ni-based superalloys are widely used in the mid-to-high temperature regimes in aircraft turbine and gas turbine engines [1,2].

The melting point of Ni, the primary element, and the stability of the γ/γ' microstructure generally determine service life-time of components such as rotor discs or turbine blades. The combustion process in turbine engines is a Carnot cycle, where the efficiency increases with operating temperature, which is essentially limited by the microstructural stability and ultimately by the melting point of the alloy. To achieve lower service cost, increase component life-time and use resources more efficiently and economically, stronger, and more resilient materials and strengthening concepts are needed.

Ni-based superalloys typically comprise a γ matrix phase, that is

* Corresponding author.
** Corresponding author at: Pico Electron Microscopy Center, Innovation Institute for Ocean Materials Characterization Technology, Center for Advanced Studies in Precision Instruments, Hainan University, Haikou 570228, Hainan, China.
*E-mail addresses:* liweijnu@126.com (W. Li), fvogel@hainanu.edu.cn (F. Vogel).
[1] These authors contributed equally to this work.

https://doi.org/10.1016/j.jallcom.2023.172929
Received 7 December 2022; Received in revised form 16 October 2023; Accepted 19 November 2023
Available online 21 November 2023

strengthened by coherent γ' precipitates. In 2013 it was shown that the formation of hierarchical microstructures can significantly improve the mechanical properties of a Ni-based superalloy [3]. Such a microstructural hierarchy is created when additional γ particles in γ' precipitates emerge [3]. The γ phase (matrix and particles) is a face centered cubic (fcc) disordered solid solution phase, designated A1 with a random atom distribution on all lattice sites. The γ' precipitate phase is an intermetallic $Ni_3Al$ or ordered phase, designated $L1_2$, where Al atoms are on the corners and Ni atoms are on the face centers of a simple cubic lattice. Thereby, γ forming elements (e.g. Cr, Co, Mo, Ru, Ru, Hf, W, Re) can substitute for Ni atoms on Ni sites (face centers) and γ' forming elements (Ti, Ta, Nb) can substitute for Al atoms on Al sites (corners).

Later, *Song et al.* associated hierarchical microstructures with extreme creep resistance in ferritic alloys [4–6]. *Antonov et al.* revealed the formation of hierarchical microstructures in a Ni-based superalloy having and elevated concentrations of refractory alloying elements (Nb, Ta, W) [7]. Recently, *Chen et al.* linked superior high-temperature tensile properties of a Ni-Co-Al-Fe-Cr-Ti-Nb-Mo-W high-entropy superalloy (HESA) containing the refractory elements Nb, Mo and W to hierarchical microstructures, surpassing that of advanced Ni-based superalloys (CMSX-4, Mar-M200) and some conventional HEAs [8]. In their study, they attributed an average increase of 113 MPa in yield strength to the HESA having a hierarchical microstructure compared to that of the HESA with the conventional microstructure.

However, hierarchical microstructures are only metastable and two metastability pathways of γ particles have been observed:

a) ***Continuous growth and split:*** Morphological transformation from spheres to plates followed by splitting of the host phase (ordered precipitate).
b) ***Growth and dissolution:*** Partial growth and coarsening of spheres followed by dissolution.

In both cases, the γ particles disappear after prolonged exposure to high temperatures [3,7,8]. To fully capitalize on the strengthening effect of hierarchical microstructures, it is necessary to thermodynamically stabilize the γ particles up to high-temperatures comparable to the intended service conditions.

Applying phase-field modeling to hierarchical microstructures in Ni-Al it was recently be shown that the lattice misfit and the interfacial energy between nanoscale γ particles and the encompassing γ' precipitates play a major role in stabilizing γ particles in γ' precipitates [9]. The conclusions of this phase-field modeling study provide suggestions for manipulation of the metastable hierarchical microstructure through the interfacial energy, solute diffusivity, supersaturation of γ' precipitates with specific γ forming elements and the γ' precipitate size [9]. Since the coarsening/dissolution kinetics are nearly proportional to the interfacial energy, it is expected that the temporal stability of γ' particles can be enhanced to 5–10 times longer durations, provided that optimum elastic strain is maintained to avoid directional coarsening [9].

This can be achieved through suitable alloy design strategies, where γ forming elements are added as they predominantly partition to the γ particle phase and thereby alter properties such as lattice parameter, interfacial energy, elastic modulus while also affecting solute diffusivity and supersaturation of γ' precipitates (with γ forming elements). Varying the content of γ forming elements in a systematic manner allows then to ascertain and tailor the stability of hierarchical microstructures, by controlling the γ particles' behavior.

However, the as-cast microstructure and micro-segregation behavior of Ni-based superalloys are sensitive to changes in composition and the homogenization treatment needs to be carefully designed with respect to homogenization temperature window and time. This is to allow dissolution of residual interdendritic eutectic while avoiding incipient melting, remove large γ' and laves phases and give appropriate time for diffusional exchange between dendrite core and interdendritic regions to homogeneously distribute all alloying elements throughout the microstructure [10,11].

Here we use the model system $Ni_{86.1}Al_{8.5}Ti_{5.4}$ with hierarchical microstructures that follow metastability pathway a) "*Continuous growth and split*" as it provides a suitable base alloy from which we developed quaternary modifications $Ni_{86.1-n}Al_{8.5}Ti_{5.4}X_n$ with X = Cr, Co, Mo, Ru, Hf, W, Re and n = 4 (except for Re where n = 2). We first study the homogenization behavior and demonstrate a simple and straight forward method for the design homogenization treatments. We further ascertain the influence of the quaternary additions on each alloys ability to form hierarchical microstructures.

## 2. Experimental

### 2.1. Alloy preparation

Polycrystalline alloys with the composition of $Ni_{82.1}Al_{8.5}Ti_{5.4}X_4$ with X = Cr, Co, Ru, Mo, W were prepared in the form of 50 g ingots using the arc-melting method in an argon atmosphere with a water-cooled copper base plate and a tungsten electrode. It is noted that a X = Re alloy (4X) showed incomplete melting and thus a $Ni_{84.1}Al_{8.5}Ti_{5.4}X_2$ alloy with X = Re (2X) was prepared. The ingots were produced from high purity Ni, Al, Ti (5N, 5N, 4N, respectively) with the purity of the additions X between 3N and 4N.

### 2.2. Heat treatment

The as-cast ingots were cut approximately parallel to the growth direction of dendrites (along a <001> direction) into slices of 2 mm thickness. The cut slices were homogenized in a vacuum tube furnace under flowing argon (80 ml $min^{-1}$). Temperature and time for each alloys' homogenization treatment was chosen based on DSC measurements and diffusion calculations considering the spacing between dendrites. All alloys were homogenized in one batch at 1275 °C for 4 h. Separate samples of the 4W and 2Re alloys were homogenized at 1275 °C for 24 h. In addition, a separate sample of the 4Hf alloy was homogenized at 1150 °C for 4 h and 24 h. All homogenization treatments were followed by quenching in iced water.

### 2.3. Characterization

The samples for light microscopy (LM), scanning electron microscopy (SEM), and wavelength dispersive spectrometry (WDS) were mechanically ground followed by polishing in three steps. The samples were polished with a diamond suspension with particle sizes of 2.5, 1 and 0.5 μm, respectively. For microstructural investigations utilizing LM and SEM, the polished samples were etched in a solution of 45 ml $H_2O$, 30 ml $HNO_3$, 30 ml HCl and 0.9 g $MoO_3$ for 10 s. Differential scanning calorimetry (DSC) was used to determine the reaction temperatures.

WDS analysis was performed using a *JXA-8100 Electron Microprobe* with 3 X-ray spectrometers operated at 15 kV. Elemental maps were acquired in the middle regions of the as-cast and homogenized samples covering an area of 500 × 500 $\mu m^2$. In addition, point measurements were taken from the dendrite core (DC) and inter-dendritic (ID) regions, with 10 points in each region of the as-cast samples. To capture subtle non-visible compositional differences between residual DC and ID regions in the homogenized samples that are not visible in a mapping, point measurements were taken in a 3 × 3 point grid array. The distance between each point (in x and y direction) was about 50–90 μm, approximately corresponding to half of the interdendritic spacing $\lambda$, as obtained from light microscopy images of the as-cast samples of each alloy.

The current used for point analyses was 20 nA, the voltage was 20 kV, and the spot size was about 1–2 μm. Pure element standards were measured prior to analysis.

TEM sample preparation was done using a *ThermoFisher Helios 5 CX* focused ion beam (FIB) instrument. Before performing the FIB lift-outs,

the orientation of the microstructure was considered to ensure a (001) orientation for the TEM sample. Thinning was done with initially 30 kV $Ga^+$ ions followed by final low kV step at 2 kV to remove surface damage.

TEM imaging was done using a *ThermoFisher Talos F200i* operated at 200 kV. Dark-field imaging was conducted with an $L1_2$ superlattice reflection.

DSC analysis was performed using a *Mettler TGA/DSC 3+* for all as-cast samples under flowing argon at 50 ml $min^{-1}$ with a heating rate of 10 K $min^{-1}$. The mass of each DSC sample was within (28 ± 2) mg.

ThermoCalc based on the CALPHAD method and ThermoCalc Software [12] and the TCNi12 Nickel -based superalloys database [13] were used to obtain reaction temperatures.

## 3. Results and discussion

### 3.1. Characterization of the as-cast conditions

Fig. 1**a**–**f** shows a series of light microscopy images of $Ni_{82.1}Al_{8.5}Ti_{5.4}X_4$ alloys with X = Cr, Co, Ru, Mo, Hf and W, respectively, and a $Ni_{84.1}Al_{8.5}Ti_{5.4}Re_2$ alloy having dendritic microstructures. For simplicity, hereafter the seven alloys will be referred to as 4Cr, 4Co, 4Ru, 4Mo, 4Hf, 4W and 2Re, respectively. For all alloys, the dendrite core (DC) region appears bright and the interdendritic region (ID) is shown in dark (except for 4Hf, where the contrast is inverted). The polycrystalline samples were cut parallel to the dendrites' growth direction, a <001> direction, exposing a longitudinal view of the dendrite cores and primary dendrite arms. The dendritic microstructure appears finer for the 4Cr, 4Hf, 4W and 2Re alloys (Fig. 1**a**, **e**, **f** and **g**) compared to that of 4Co, 4Ru and 4Mo alloys (Fig. 1**b**, **c** and **d**). A small number of pores is present in all microstructures, with the 4Hf sample showing a higher degree of randomly distributed porosity (Fig. 1**e**).

#### 3.1.1. Diffusion distance (dendritic microstructure)

To further quantify dendritic segregation and the diffusion distance which the alloying elements need to overcome for homogenization, the interdendritic spacing, $\lambda$ is considered. Fig. 2 shows a schematic representation of the dendritic microstructure as observed in Fig. 1**,** with dendrites growing in [001] direction (longitudinal view). In the three-dimensional view in Fig. 2**a** the interdendritic distance between two dendrite cores is indicated as $\lambda$. To obtain the diffusion distance $x$ between the middle of DC and ID regions, the transversal view is considered schematically in Fig. 2**b**, whereby the dendrites are assumed to be arranged in a square grid.

We derive $x$ from $\lambda$ as.

$$x = (\lambda_{avg}/2)^{0.5} \quad (1)$$

with $\lambda_{avg}$ as the average from $n$ measurements of $\lambda_n$ ($n = 50$ in this work).

$$\lambda_{avg} = (\lambda_1+\lambda_2+\lambda_n)\, n^{-1} \quad (2)$$

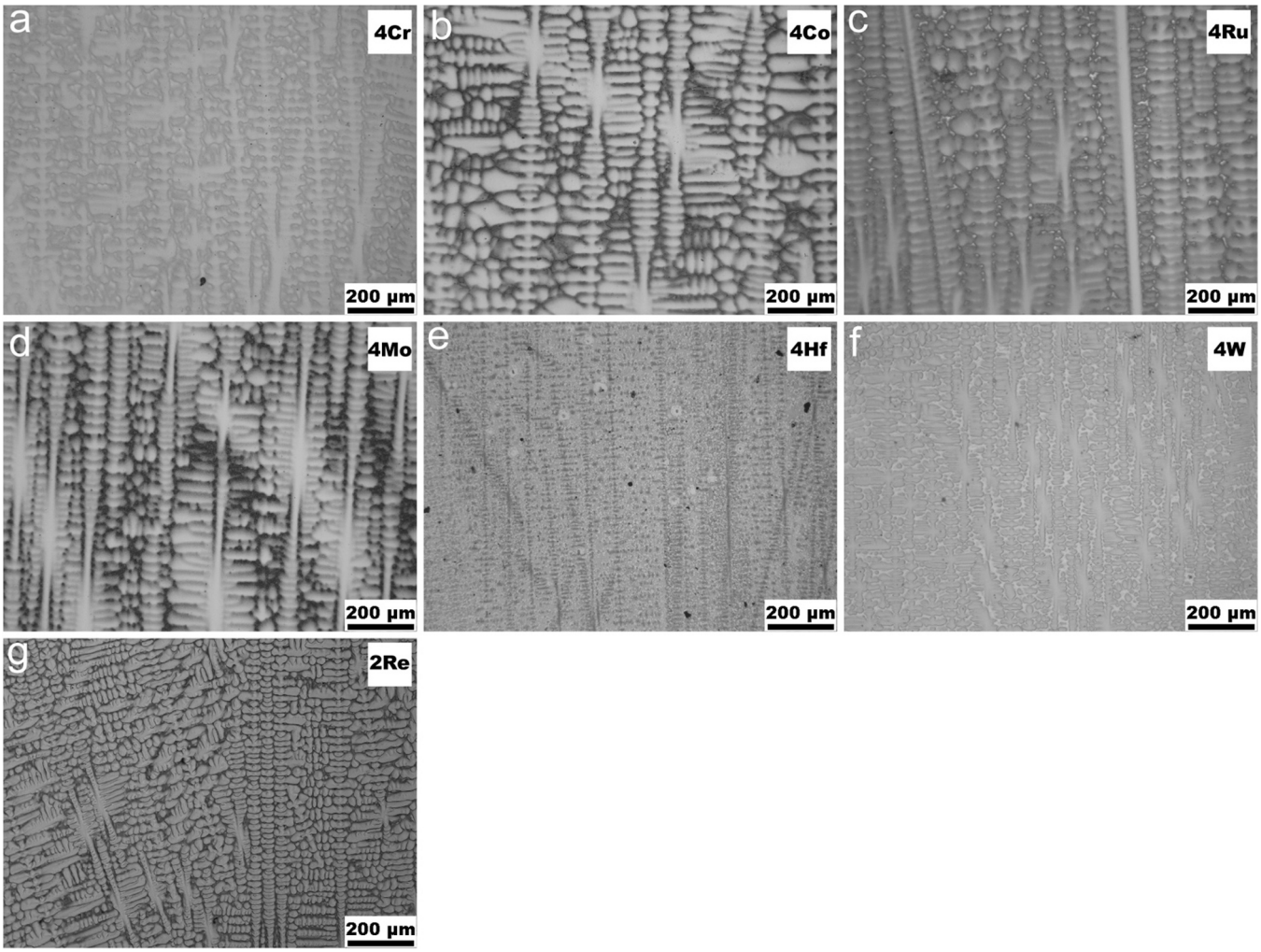


**Fig. 1.** Light microscopy images of the dendritic microstructure of $Ni_{82.1}Al_{8.5}Ti_{5.4}X_4$ alloys with X = Cr, Co, Ru, Mo, Hf and W. (**a**) 4Cr, (**b**) 4Co, (**c**) 4Ru, (**d**) 4Mo, (**e**) 4Hf, (**f**) 4 W and (**g**) 2Re.

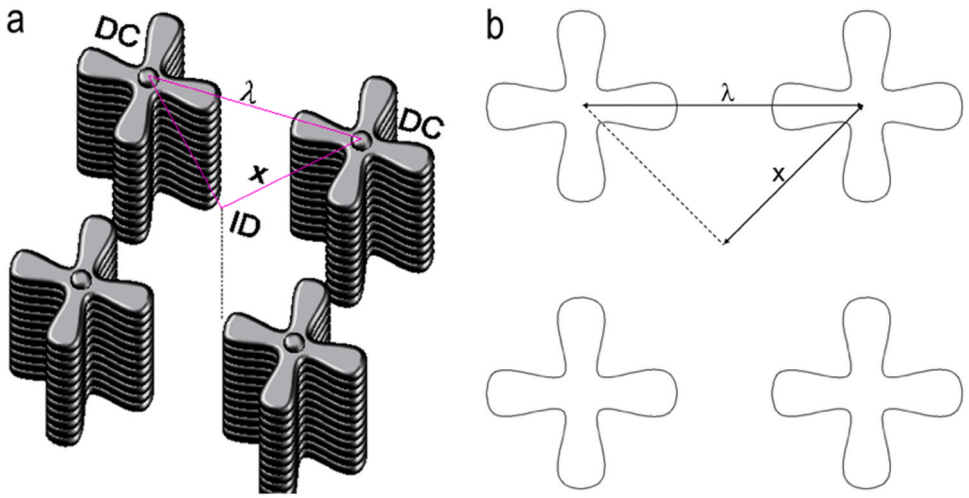


**Fig. 2.** (**a**) 3D schematic representation of dendrites illustrating the diffusion distance x between dendrite cores (DC) and the inter-dendritic (ID) regions. (**b**) *x* is illustrated in a <001> perspective (transversal view) assuming a regular grid arrangement of dendrites.

The results for $\lambda_{avg}$ and *x* of all alloys are given in Table 1 and will be utilized later for diffusion calculations.

Obtaining average values for all alloys shows that $\lambda$ for the 4Cr, 4Co, 4Ru and 4Mo alloys is around 100–130 μm, whereas the 4Hf, 4 W and 2Re alloys are in the range of 50–80 μm. Single crystalline Ni-based superalloys cast using the Bridgman method typically show $\lambda$ values between 200 and 400 μm [14–17]. The spacing between dendrites increases with decreasing solidification speed or withdrawal rate during the SX casting process [18,19]. The experimental alloys in the present study were prepared by arc melting, where the bottom of the crucible is a chilled copper plate and thus the solidification speed is much faster, leading to smaller $\lambda$ values.

### 3.1.2. *Temperature selection for homogenization*

Fig. 3**a** highlights DSC heating profiles for the 4Cr, 4Co, 4Ru, 4Mo, 4Hf, 4 W and 2Re alloys (quaternary) of a segment between 600 and 1500 °C. For reference, the profile of the ternary $Ni_{86.1}Al_{8.5}Ti_{5.4}$ base alloy is also given. It is noted that the quaternary additions X are balanced with the Ni content. Generally, the γ' dissolution occurs between 800 °C and 1200 °C, however the width of this window varies greatly among the alloys. The reaction temperatures obtained from DSC profiles (solid symbols) in Fig. 3**a** and ThermoCalc (open symbols) are compared in Fig. 3**b**, where the γ' solvus temperature (blue circles), the alloy's solids (red triangles) and liquidus (grey squares) temperature are shown. In addition, the onset of γ' dissolution from DSC is indicated (orange diamonds).

The lowest onset of γ' dissolution is found at ~800 °C for the base, 4Mo and 4Ru alloys (Fig. 3**b**), with the end of γ' dissolution below 1250 °C. The 4Cr, 4Co,4W and alloys' onset of γ' solution occurs at ~1000 °C, with the end of γ' dissolution at ~1200 °C for the 4Cr and 2Re alloy and lower, at ~1100 °C for the 4Co, 4Hf and 4W alloys. The γ'

**Table 1**
Quantitative results for the average interdendritic spacing $\lambda_{avg}$ and the caclulated diffusion distance x obtained for the 4Cr, 4Co, 4Ru, 4Mo, 4Hf, 4W and 2Re alloys in as-cast condition as shown in Fig. 1**a–g**, respectively.

| Alloy | λ (μm) | x (μm) |
|---|---|---|
| 4Cr | 114 ± 66 | 81 ± 47 |
| 4Co | 120 ± 95 | 85 ± 67 |
| 4Ru | 115 ± 57 | 81 ± 40 |
| 4Mo | 106 ± 51 | 75 ± 36 |
| 4Hf | 66 ± 43 | 47 ± 30 |
| 4 W | 68 ± 31 | 48 ± 22 |
| 2Re | 81 ± 63 | 57 ± 45 |

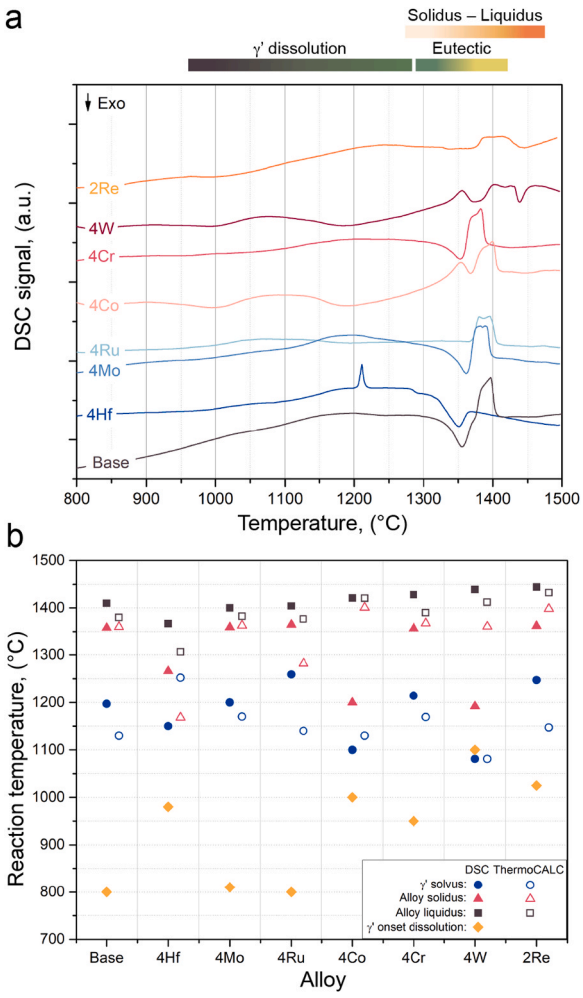


**Fig. 3.** (**a**) DSC heating profiles for the section between 600 and 1500 °C, obtained at a heating rate of 10 K $min^{-1}$. (**b**) Comparison of reaction temperatures from DSC (solid symbols) and ThermoCALC (open symbols) of the ternary base ($Ni_{86.1}Al_{8.5}Ti_{5.4}$) and the quaternary 4Cr, 4Co, 4Ru, 4Mo, 4Hf, 4W and 2Re alloys of the as-cast condition.

solvus temperatures of our experimental alloys are lower compared to compositionally more complex commercially used SX Ni-based superalloys, e.g., second generation superalloy CMSX-4 which shows a γ' solvus temperature around ~1290 °C [20,21]. The higher γ' solvus temperature of these more complex alloys is attributed to the addition of further γ' forming elements, i.e., Ta, which has a higher melting point compared to Al and Ti (the only γ' formers in our experimental alloys) [22].

For the 4Hf alloy, the peak at ~1200 °C is attributed to the melting of a $Ni_5Hf$ containing eutectic phase. Peaks from residual inter-dendritic eutectic phase are also observed for the 4Co and 4W alloys between ~1200 °C and ~1350 °C, with the onset dragging from ~1200 °C to ~1325 °C before the peak appears at ~1350 °C. Solidus and liquidus temperatures lie between ~1350 °C and ~1440 °C for the 4Cr, 4Mo, 4Ru, 4Co, 4W and 2Re alloys. The base alloy falls well in the middle of that range. The 4Hf alloy shows the lowest solidus and liquidus temperatures with ~1200 °C and 1350 °C, respectively, and the sharp peak is indicative phase separation and formation of low melting point phases during heating.

The reaction temperatures obtained from DSC profiles inform the selection of a temperature for the homogenization of our quaternary alloys, which ideally is a batch process to improve efficiency. A summary of all reaction temperatures is given in Fig. 3**b**). The important temperatures are the γ' dissolution temperature (γ' solvus, blue circles) and the alloys' solidus temperature (red triangles) in Fig. 3**b**. In this interval, for the 4Cr, 4Mo, 4Ru, 4Co, 4W and 2Re (and base) alloys, there is a temperature window of 1250–1350 °C.

The γ' dissolution temperatures from Thermo-Calc are in good agreement for the 4Mo and 4W alloys (within 10 °C), underestimated for the base, 4Co, 4Ru and 2Re alloys (within 50–100 °C) and underestimated for the 4Cr and 4Hf alloys (within 70–100 °C). The alloy's solidus temperatures between DSC and ThermoCalc are in good agreement except for the 4Co (+40 °C), 4Ru (−80 °C), 4Hf (−200 °C) and 2Re (+50 °C) alloys. The alloy's liquidus temperatures from DSC are generally slightly higher (10–50 °C) compared to Thermo-Calc, with the 4Mo alloy being marginally underestimated and the 4Hf alloy by ~70 °C. Eutectic phases were not predicted by ThermoCalc.

For these alloys we chose 1275 °C as the homogenization temperature, being above the ending temperature for dissolution of γ' to dissolve γ' precipitates and homogeneously distribute all alloying elements in the solid solution γ phase, stable at this temperature. Further, 1275 °C leaves enough safety margin to the solidus temperatures to avoid incipient melting of the residual eutectic observed for the 4Co and 4W alloys. Residual eutectic forms in the inter-dendritic regions at the end of solidification, because of continuous decomposition of the melt during solidification [22–24]. When the degree of decomposition is large enough, the eutectic composition can be achieved, often introducing areas with a typical lamellar eutectic structure in the inter-dendritic regions [22–24]. The low melting point of the eutectic phase poses a challenge for the design of a homogenization treatment and often requires complex temperature profiles or ramps for gradual dissolution without incipient melting [22–24].

According to our DSC data, the 4Hf alloy requires a lower homogenization temperature window between 1100 °C and 1150 °C. We chose 1150 °C to maximize diffusion kinetics and allow for an economic homogenization process.

### 3.1.3. Time selection for homogenization

To estimate the time $t$ necessary for homogenization based on the diffusion distance $x$ (Table 1) and the homogenization temperatures ($T = 1275$ °C for 4Cr, 4Co, 4Ru, 4Mo, 2Re, and $T = 1150$ °C for 4Hf) chosen for each alloy, we predict the residual segregation index as function of the diffusion distance $x$, the homogenization temperature $T$ and diffusion parameters for each element (Table 2).

The compositional difference between DC and ID regions is commonly known as micro segregation, which is characterized by the

**Table 2**
Diffusion parameters. The frequency factor for volume diffusion $D_0$ and the activation energy for diffusion $Q$ of each element in nickel-based superalloys. All values taken from the literature (see references).

| Element | Label Fig. 4 | $D_0$ ($m^2\ s^{-1}$) | Q (J $mol^{-1}$) | Material/Phase | Reference |
|---|---|---|---|---|---|
| Ni | Ni | $1.00 \times 10^{-03}$ | 271960 | Ni / Ni-45Al (at %) diffusion couple | *Janssen 1973* [25] |
| Al | Al | $1.50 \times 10^{-03}$ | 282000 | γ/γ' diffusion couple | *Karunaratne et al. 2001* [26] |
| Ti | Ti | $3.70 \times 10^{-04}$ | 272000 | γ/γ' diffusion couple | *Karunaratne et al. 2001* [26] |
| Cr | Cr 1 | $2.02 \times 10^{-05}$ | 260000 | Pure Ni coated with pure Cr (5 nm) | *Gheno et al. 2018*[27] |
| | Cr 2 | $5.20 \times 10^{-04}$ | 289000 | Ni / Ni-5.06Cr (at%) diffusion couple | *Jung et al. 1992*[28] |
| | Cr 3 | $1.10 \times 10^{-04}$ | 272400 | Inconel-600 coated with pure Cr | *Dpruthi et al. 1977*[29] |
| Co | Co 1 | $2.77 \times 10^{-04}$ | 284787 | n.a. | *Vladimirov et al. 1978* [30] |
| | Co 2 | $2.20 \times 10^{-04}$ | 282000 | Ni / Ni-4.85Co (at%) diffusion couple | *Jung et al. 1992*[28] |
| | Co 3 | $2.97 \times 10^{-04}$ | 281605 | First principles calculations | *Wu et al. 2012* [31] |
| Ru | Ru 1 | $2.48 \times 10^{-04}$ | 304400 | Ni / Ni-2.97Ru (at%) diffusion couples | *Karunaratne et al. 2003* [32] |
| | Ru 2 | $6.20 \times 10^{-05}$ | 288800 | Ni / Ni-6.06Ru (at%) diffusion couple | *Karunaratne et al. 2003* [32] |
| | Ru 3 | $5.99 \times 10^{-05}$ | 291270 | Ni / Ni-5Co-5Ru (at%) diffusion couple | *Mabruri et al. 2007*[33] |
| | Ru 4 | $2.38 \times 10^{-04}$ | 302280 | First principles calculations | *Wu et al. 2012* [31] |
| Mo | Mo 1 | $1.15 \times 10^{-04}$ | 281300 | Ni / Ni-6.5Mo (at%) diffusion couples | *Karunaratne et al. 2005* [34] |
| | Mo 2 | $1.56 \times 10^{-04}$ | 282500 | Ni / Ni-5Mo (at %) diffusion couple | *Heijwegen et al. 1973* [35] |
| | Mo 3 | $2.30 \times 10^{-04}$ | 285000 | Ni / Ni-9Mo (at %) diffusion couple | *Ugaste et al. 1972*[36] |
| Hf | Hf 1 | $5.18 \times 10^{-05}$ | 242788 | Ni/ Ni-0.16Hf and Ni/ Ni-1.18Hf (at%) diffusion couple | *Bergner et al. 1972*[37] |
| | Hf 2 | $8.95 \times 10^{-02}$ | 362166 | Ni / $Ni_5Hf$ diffusion couple | *Ma et al. 1996* [38] |
| | Hf 3 | $1.20 \times 10^{17}$ | 858720 | $Ni_3Al$ / $Ni_5Hf$ diffusion couple | *Ma et al. 1996* [38] |
| W | W 1 | $2.07 \times 10^{-04}$ | 304040 | Ni / Ni-4 W (at %) diffusion couple | *Walsh et al. 1969*[39] |
| | W 2 | $2.10 \times 10^{-04}$ | 302510 | First principles calculations | *Wu et al. 2012* [31] |
| | W 3 | $8.00 \times 10^{-06}$ | 264000 | Ni / Ni-3.43 W (at%) diffusion couples | *Karunaratne et al. 2000* [40] |
| | W 4 | $2.79 \times 10^{-05}$ | 282130 | Calculated with CALPHAD-type approach | *Campbell et al. 2002*[41] |
| | W 5 | $9.78 \times 10^{-06}$ | 294140 | First principles calculations | *Fan et al. 2015* [42] |
| Re | Re 1 | $8.20 \times 10^{-07}$ | 254380 | Ni / Ni-3.38Re (at%) diffusion couples | *Karunaratne et al. 2000* [40] |

(*continued on next page*)

**Table 2** (*continued*)

| Element | Label Fig. 4 | $D_0$ ($m^2$ $s^{-1}$) | Q (J $mol^{-1}$) | Material/Phase | Reference |
|---|---|---|---|---|---|
| | Re 2 | $1.05 \times 10^{-03}$ | 343180 | Ni / Ni-5Co-5Re (at%) diffusion couple | *Mabruri et al. 2007*[33] |
| | Re 3 | $3.28 \times 10^{-06}$ | 278820 | Calculated with CALPHAD-type approach | *Campbell et al. 2002*[41] |
| | Re 4 | $3.77 \times 10^{-06}$ | 271640 | Ni / Ni-5Al-5Re (at%) diffusion couple | *Mabruri et al. 2006*[43] |

residual segregation index $\delta$ for each alloying element with non-uniform distribution:

$$\delta = (C^t_{DC}\text{-}C^t_{ID}) \,/\, (C^0_{DC}\text{-}C^0_{ID}) \tag{3}$$

where $C^0_{DC}$ and $C^0_{ID}$ are the element concentrations in DC and ID regions of the as-cast alloy, while $C^t_{DC}$ and $C^t_{ID}$ are the element concentrations of DC and ID regions after homogenization, respectively. Using microstructural parameters, such as the distance between the center of the DC and ID regions, $x$ (derived form $\lambda$ (Eq. 1), listed in Table 1), and diffusion parameters (Table 2), the time $t$ required to achieve a certain degree of homogenization at a given temperature $T$ scales $\delta$ as follows:

$$\ln \quad \delta = -\frac{4\pi^2}{x^2} \quad D_0 \exp\left(-\frac{Q}{RT}\right) t \tag{4}$$

*where* $D_0$ is the frequency factor for volume diffusion, $Q$ the activation energy and $R$ the gas constant.

In Fig. 4, the calculated evolution of $\delta_{(t)}$ with time at a homogenization temperature of 1275 °C (4Cr, 4Co, 4Ru, 4Mo and 2Re, Fig. 4**a**–**d, f** and **g**) or 1150 °C (4Hf, Fig. 4**e**) gives a prediction of the homogenization behavior. The $\delta_{(t)}$ profiles for Ni, Al and Ti as dark blue, blue and turquoise lines (cold colors), respectively. The $\delta_{(t)}$ profiles for quaternary additions X in each subfigure are plotted for various diffusion parameters ($D_0$ and $Q$) and shown in red and orange shades. The interdendritic spacing $\lambda$ is different for each alloy, hence the variation of $\delta_{(t)}$ for Ni, Al and Ti for each alloy. Typically, $\delta$ values $< 20\%$ indicate a sufficient degree of homogenization ($\delta = 20\%$ is indicated by a grey dashed line).

Diffusion parameters not only depend on the circumstances under which they were acquired but also on alloy and phase composition, concentration gradients, crystal structure and order, i.e., diffusion kinetics are faster in a disordered solid solution (γ phase matrix) compared

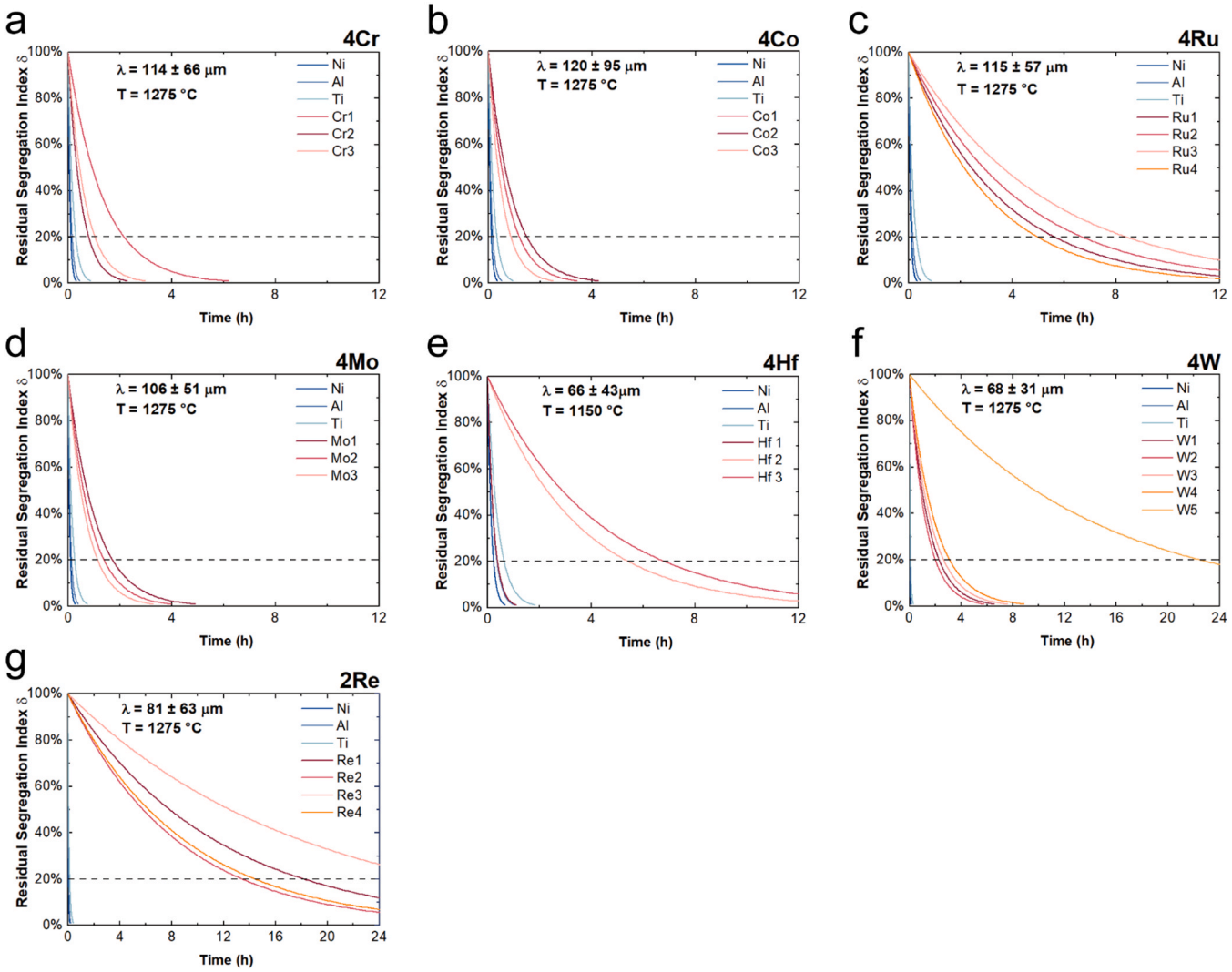


**Fig. 4.** Theoretical residual segregation index $\delta_{(t)}$ for the 4Cr, 4Co, 4Ru, 4Mo, 4Hf, 4W and 2Re alloys (for Ni, Al, Ti, and Cr, Co, Mo, Ru, Hf, W or Re) at a homogenization temperature of 1275 °C (4Cr, 4Co, 4Ru, 4Mo, 4W and 2Re) or 1150 °C (4Hf). $\delta_{(t)}$ is calculated based on Eq. (4) using $x$ values (derived from $\lambda$) for each alloy (Table 1) and diffusion parameters (Table 2).

to ordered precipitates (γ' phase precipitates). Hence, for our calculation of $\delta_{(t)}$ profiles, we used at least three different diffusion parameters from the literature for each element (Table 2).

In Fig. 4, the $\delta_{(t)}$ profiles for Ni, Al and Ti in all alloys reveal $\delta_{(t)} < 20\%$ within t < 1 h for all alloys. Considering the quaternary elements X added to each alloy, the $\delta_{(t)}$ profiles in Fig. 4 indicate that Cr, Co, Mo and W achieve $\delta_{(t)} < 20\%$ within t = 4 h at 1275 °C, while Ru requires t = 4–8 h and Re t = 12–20 h. The $\delta_{(t)}$ profiles of Hf at 1150 °C predicts $\delta_{(t)} < 20\%$ within t < 2 h.

A summary of suitable homogenization parameters chosen based on DSC data (temperature) and $\delta_{(t)}$ profiles (time) is given in Table 2. Homogenization of our experimental quaternary alloys was carried out according to these parameters..

### 3.2. Analysis of micro segregation (EPMA)

To reveal the element distribution in the dendritic microstructure of the as-cast and homogenized states (1275 °C / 4 h and 24 h, 1150 °C / 4 h and 24 h), an electron probe micro-analyzer (EPMA) data was used to obtain elemental mappings and point measurements from DC and ID regions, for all alloys (4Cr, 4Co, 4Ru, 4Mo, 4Hf, 4W and 2Re). The alloys in this section are grouped and organized according to their homogenization behavior:

As a fully homogeneous element distribution is achieved for the 4Cr, 4Co, 4Mo and 4Ru alloys after 1275 °C / 4 h, thus EPMA elemental mappings are only shown for the 4Cr alloy in as-cast (Fig. 5**a-i** – **c-i**) and homogenized condition (Fig. 5**a-ii** – **c-ii**). In Fig. 6**a-i** – **e-i**), elemental mappings of the 4W alloy (as-cast) are shown as residual Ti and W segregation is present in ID regions after 1275 °C / 4 h (Fig. 6**a-ii** – **e-ii**) and a fully homogeneous state is only achieved after 1275 °C / 24 h (Fig. 6**a-iii** – **e-iii**). In Fig. 7**a-i** – **e-i**, elemental mappings of the 2Re alloy (as-cast), show dendritic segregation even after 1275 °C / 4 h (Fig. 7**a-ii** – **e-ii**) with full homogenization achieved after 1275 °C / 24 h (Fig. 7**a-iii** – **e-iii**). Lastly, in Fig. 8**a-i** – **e-i**, elemental mappings of the 4Hf alloy (as-cast) are shown, with remaining segregation after 1150 °C / 4 h (Fig. 8**a-ii** – **e-ii**) and 1150 °C / 24 h (Fig. 8**a-iii** – **e-iii**).

We note that, although the DSC data for the 4Co alloy in the as-cast state (Fig. 3) suggests the presence of eutectic, however the SEM-BSE images and EPMA mappings did not clearly indicate eutectic phases in ID regions.

The results of quantitative analyses (point measurements) of all alloys in as-cast and homogenized conditions are presented in Table 4.

#### 3.2.1. 4Cr (and 4Co, 4Mo and 4Ru): Fully homogenized after 1275 °C / 4 h

For the as-cast state of the 4Cr alloy in Fig. 5**a-i**, the element sensitive SEM back-scatter electron (BSE) image comprises a bright (left) and a dark (right) region, corresponding to two different grains (electron channeling contrast). Subtle traces of a dendritic microstructure appear within each grain, with DC regions visible (bright, corresponding to heavier elements, i.e., Ni). Ti shows the strongest segregation behavior with a tendency to accumulate in the interdendritic regions (Fig. 5**b-i**). The distribution of Cr appears nearly homogeneous, with a slight depletion in ID regions as indicated by a red arrow (Fig. 5**c-i**). EPMA mappings of Ni and Al do not show signs of segregation and are omitted for brevity. Full homogenization of the 4Cr (and 4Co, 4Mo and 4Ru) is achieved after 1275 °C / 4 h (Fig. 5**a-ii – c-ii**).

**Table 3**
Homogenization parameters for the Ni-Al-Ti-X alloys (with X = Cr, Co, Ru, Mo, Hf, W or Re). Temperature and time chosen based on microstructure analysis (Fig. 1) to determine $\lambda$ (and $x$), and calculation of the relative segregation index $\delta_{(t)}$ profiles (Fig. 4) using diffusion parameters from Table 2.

| Temperature | 1275 °C | | 1150 °C | |
|---|---|---|---|---|
| Alloy | Time | | Time | |
| 4Cr | 4 h | | | |
| 4Co | 4 h | | | |
| 4Ru | 4 h | | | |
| 4Mo | 4 h | | | |
| 4Hf | | | 4 h | 24 h |
| 4 W | 4 h | 24 h | | |
| 2Re | 4 h | 24 h | | |

#### 3.2.2. 4 W: Residual inter-dendritic eutectic after 1275 °C / 4 h and full homogenization after 24 h

Fig. 6 shows the SEM-BSE images and EPMA mappings of the 4W alloy. A typical dendritic microstructure is visible in the as-cast state, whit DC and ID regions (bright and dark, respectively) visible in the SEM-BSE image (Fig. 6**a-i**). Segregation of Ni is not observed (Fig. 6**b-i**) and Al appears to be slightly enriched in ID regions (Fig. 6**c-i**). Ti and W show strong segregation towards ID and DC regions, respectively (Fig. 6**d-i** and **e-i**). After homogenization at 1275 °C / 4 h, residual eutectic is present in the ID regions, visible in dark in the SEM-BSE image, indicating accumulation of light elements Al and Ti (marked by red arrows in Fig. 6**a-ii – e-ii**). As in the as-cast state, a homogeneous distribution of Ni is observed. The mappings of Al and Ti confirm the segregation of light elements to residual eutectic ID regions (Fig. 6**c-ii and d-ii**), while W shows the opposite behavior (Fig. 6**e-ii**). Presence of a eutectic phase is also revealed by DSC data, by a peak with a maximum around ~1350 °C (Fig. 3**a**). In contrast, our prediction of the homogenization behavior of W in the 4W alloy (Fig. 4**f**) shows full homogenization should be achieved after 1275 °C / 4 h for $\delta_{(t)}$ profiles based on experimentally obtained diffusion parameters for W (W1–3) and calculated using the CALPHAD approach (W4). For W diffusion parameters determined by first principle calculations (W5, [42]), we obtain $\delta_{(t)} < 20\%$ after 1275 °C / 24 h, which is in excellent agreement to our experimental data shown in Fig. 6**a-iii – e-iii**, where complete homogenization is achieved after 1275 °C / 24 h.

#### 3.2.3. 2Re: Residual dendritic segregation after 1275 °C / 4 h and full homogenization after 24 h

Fig. 7 shows the SEM-BSE images and EPMA mappings of the 2Re alloy in as-cast and homogenized conditions (1275 °C for 4 h or 24 h). The as-cast state shows dendritic segregation with DCs and primary dendrite arms appearing bright in BSE contrast (Fig. 7**a-i**), indicative of elements with a higher z number, i.e. Ni and Re. In the EPMA mappings, Ni appears to be enriched in the DC regions (Fig. 7**b-i**), Al and Ti are enriched in the ID regions (Fig. 7**c-i** and **d-i**). Re exhibits a very strong segregation towards DC regions (Fig. 7**e-i**). As predicted by our calculation of $\delta_{(t)}$ profiles for the 2Re alloy and the homogenization behavior of Re (Fig. 4**g**), 1275 °C / 4 h is not sufficient to achieve homogenization. We observe a more homogeneous distribution of elements compared to the as-cast state, but remaining segregation is still present (Fig. 7**a-ii – e-ii**). After 1275 °C / 24 h, full homogenization is achieved which agrees to our calculated $\delta_{(t)}$ profiles using experimentally obtained diffusion parameters Re1 [40], Re2 [33] and Re4 [43] with $\delta_{(t)} < 20\%$ after t = 14–20 h. For diffusion parameter set Re3, which was determined based on a CALPHAD-type approach [41], we obtain $\delta_{(t)} < 20\%$ after t > 24 h, slightly overestimating the required time.

#### 3.2.4. 4Hf: Remaining segregation after 1150 °C / 4 h and 24 h

Fig. 8 highlights a complete set of EPMA mappings for Ni, Al, Ti and Hf for the 4Hf alloy in the as-cast and homogenized states (1150 °C for 4 h or 24 h). The BSE image of the as-cast state Fig. 8**a-i** comprises a dendritic microstructure with strong contrast between DC (dark) and ID regions (bright), revealing the accumulation of heavier elements in the ID regions. The DC region appears enriched in Ni (Fig. 8**b-i**), while Al and Ti show a tendency to segregate into ID regions (Fig. 8**c-i** and **d-i**). Hf is almost exclusively found in ID regions (Fig. 8**e-i**). The ID regions are further subdivided into two regions: an interdendritic region rich in Al, Ti and Hf and an interdendritic eutectic regions (ID-EUT) rich in Hf while depleted in Ni, Al and Ti. An enlarged view of a representative

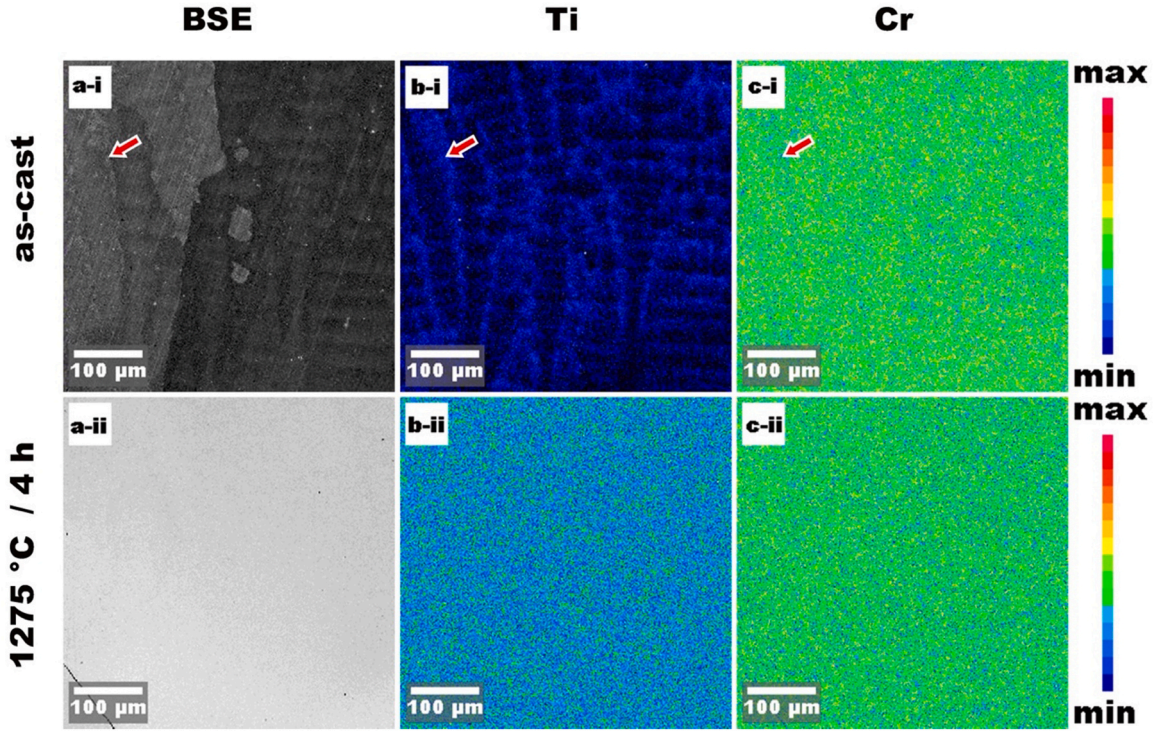


**Fig. 5.** The **4Cr** alloy**:** SEM-BSE images (**a-i** and **a-ii**) and corresponding EPMA elemental mappings of Ti (**b-i** and **b-ii**) and Cr (**c-i** and **c-ii**). The as-cast state (top row) and the homogenized state, 1275 °C / 4 h (bottom row) are shown. The same location in an interdendritic region (ID) is marked by red arrows.

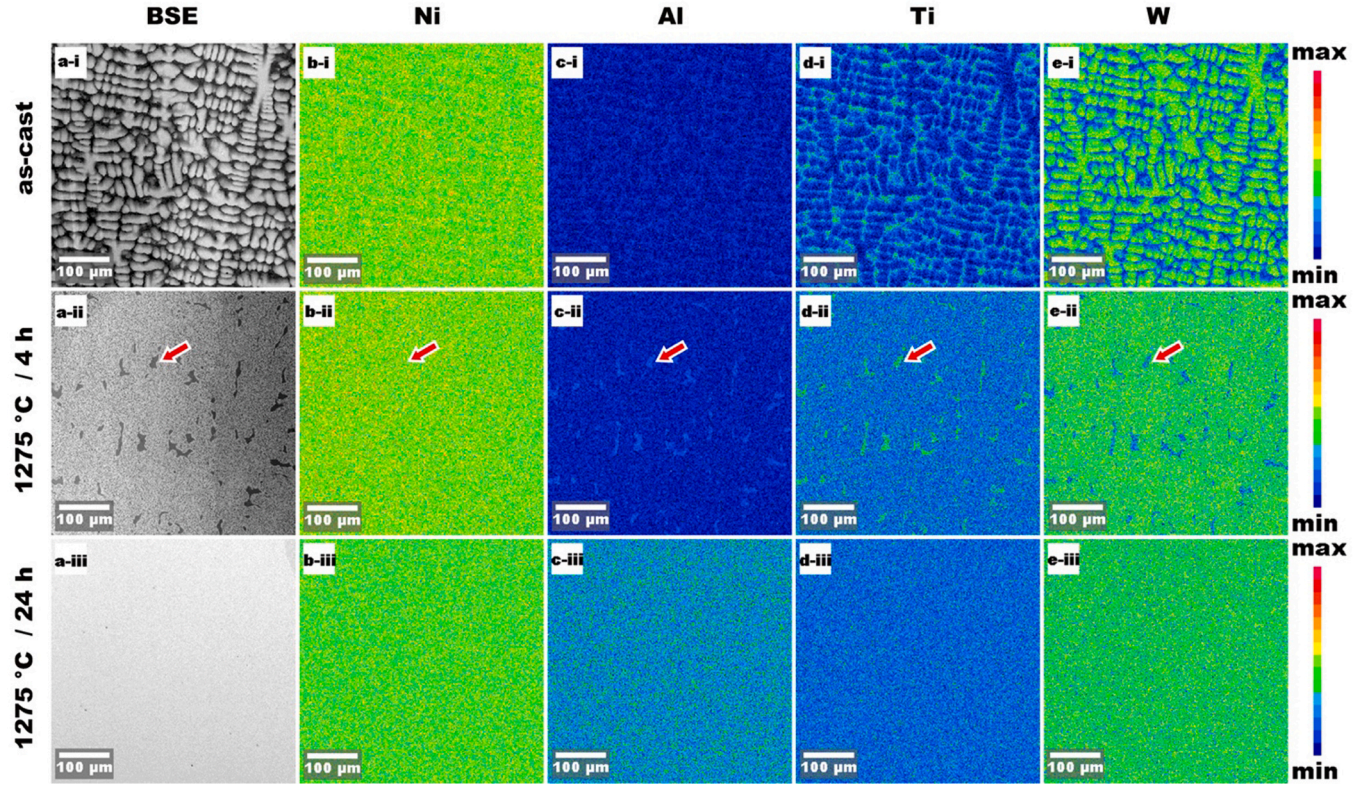


**Fig. 6.** The **4W alloy:** SEM-BSE images (**a-i – iii**) and corresponding EPMA elemental mappings of Ni (**b-i – iii**), Al (**c-i – iii**) Ti (**d-i – iii**) and W (**e-i – iii**). The as-cast state (top row, i) and the homogenized state: 1275 °C / 4 h (midle row, ii) and 1275 °C / 24 h (bottom row, iii) are shown.

area, showing DC (dark), ID (grey) and ID-EUT (white/grey lamellar) regions is presented in Fig. 9. The lamellar structure in ID-EUT is attributed to a eutectic reaction forming a eutectic phase with the Ni+Hf-rich layer corresponding to $Ni_5Hf$.

After homogenization at 1150 °C / 4 h, the BSE image (Fig. 8**a-ii**) and the EPMA mappings (Fig. 8**a-ii** – **e-ii**) still clearly show dendritic

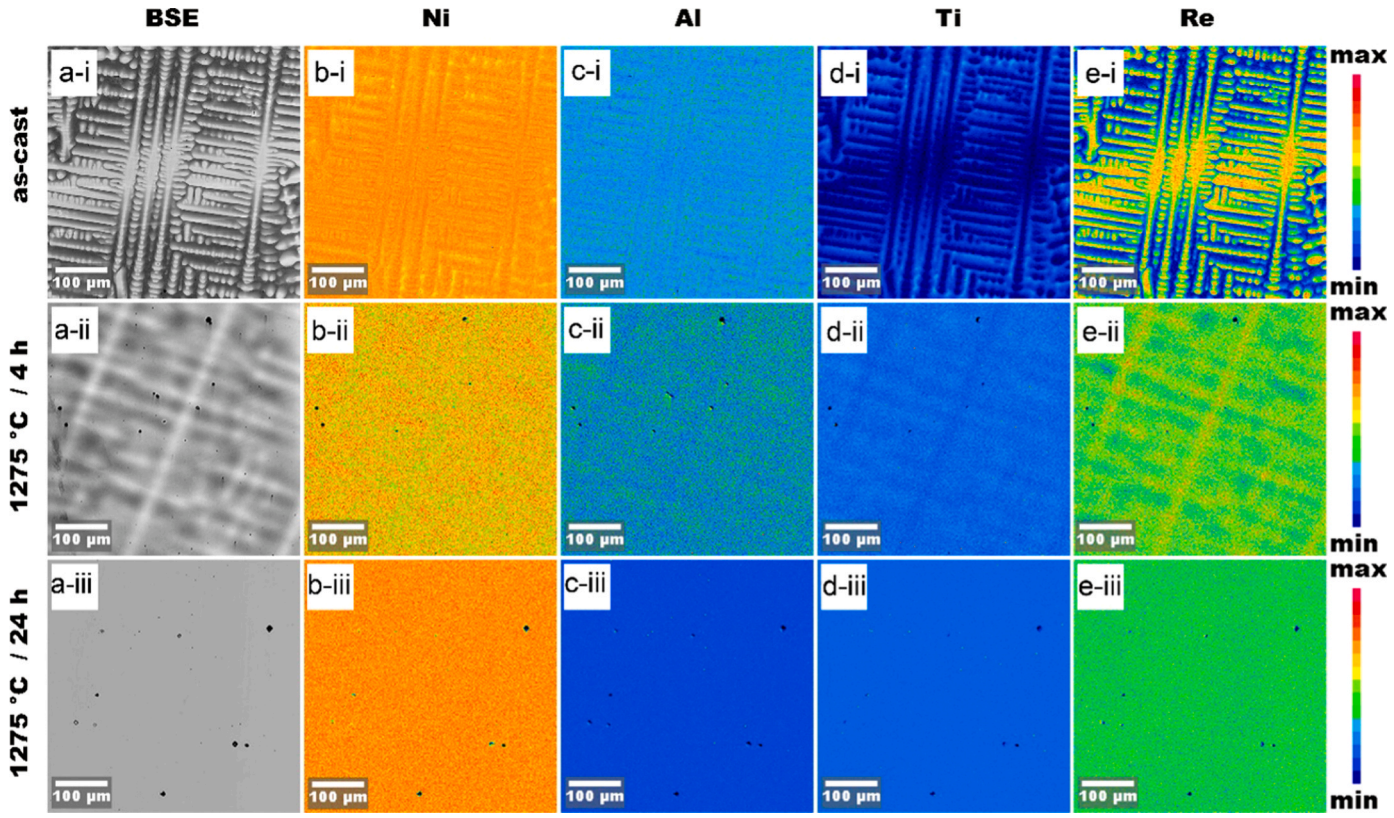


**Fig. 7.** The **2Re** alloy**:** SEM-BSE images (**a-i – iii**) a corresponding EPMA elemental mappings of Ni (**b-i – iii**), Al (**c-i – iii**) Ti (**d-i – iii**) and Re (**e-i – iii**). The as-cast state (top row, **i**) and and the homogenized state,1275 °C / 4 h (middle row, **ii**) and 1275 °C / 24 h (bottom row, iii) are shown.

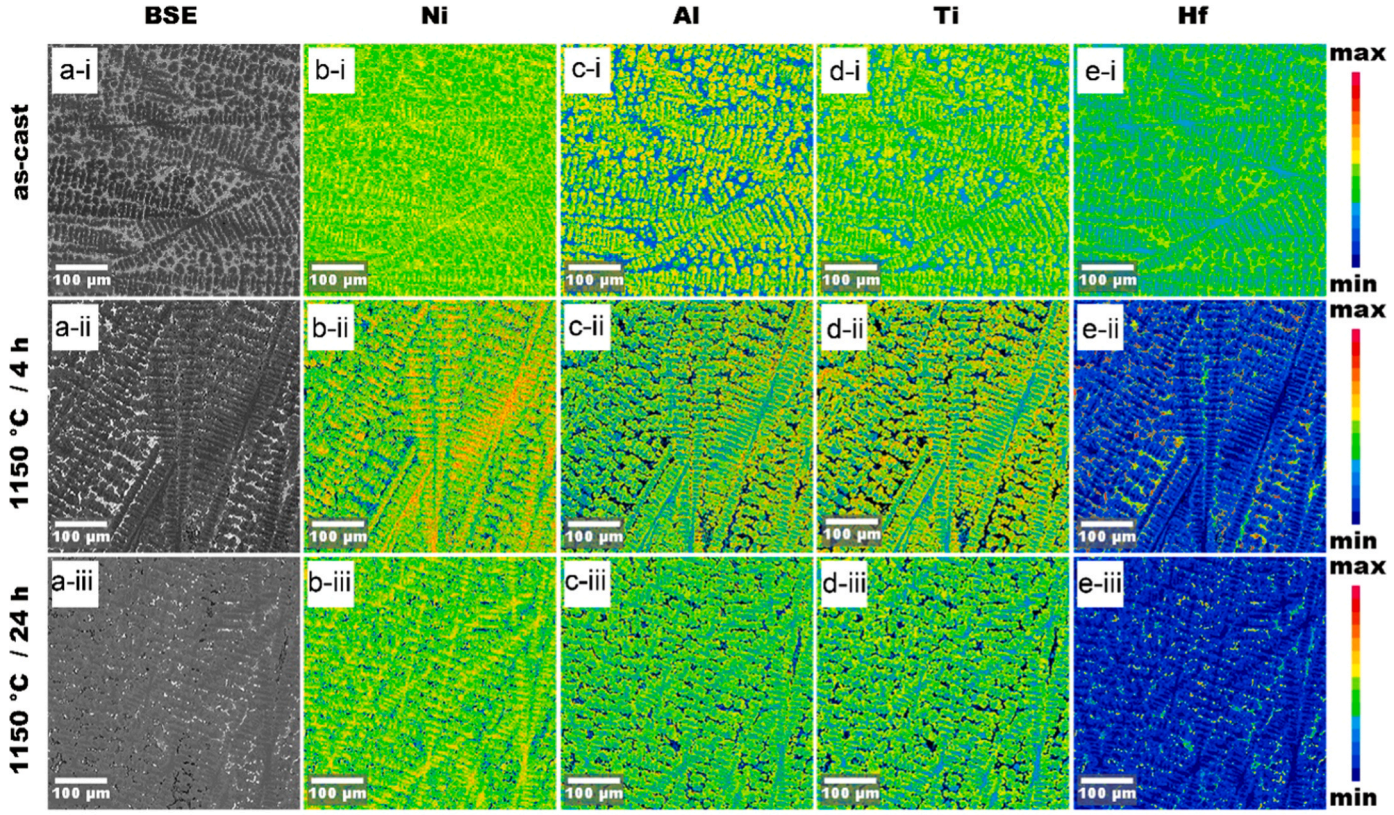


**Fig. 8.** The **4Hf** alloy: SEM-BSE images (**a-i – iii**) and corresponding EPMA elemental mappings of Ni (**b-i – iii**), Al (**c-i – iii**) Ti (**d-i – iii**) and Hf (**e-i – iii**). The as-cast state (top row) and the homogenized states,1150 °C / 4 h (midle row) and 1150 °C / 24 h (bottom row) are shown.

**Table 4**
EPMA analysis of 4Cr, 4Co, 4Ru, 4Mo, 4Hf, 4W and 2Re alloys in as-cast state. Concentrations of dendrite core (DC) and interdendritic (ID) regions are given in at%. Errors are standard deviations 2$\sigma$.

| As-cast | | | | | |
|---|---|---|---|---|---|
| | | Concentration, (at%) | | | |
| Alloy 4X | Region | Ni | Al | Ti | X |
| 4Cr | DC | 82.66 ± 0.69 | 8.47 ± 0.23 | 4.62 ± 0.90 | 4.25 ± 0.15 |
| | ID | 80.91 ± 1.14 | 7.84 ± 0.78 | 7.16 ± 1.35 | 4.09 ± 0.30 |
| 4Co | DC | 82.86 ± 0.75 | 8.43 ± 0.28 | 4.39 ± 0.83 | 4.31 ± 0.25 |
| | ID | 76.96 ± 1.76 | 6.19 ± 0.89 | 12.89 ± 1.76 | 3.95 ± 0.13 |
| 4Ru | DC | 82.58 ± 0.55 | 8.44 ± 0.30 | 4.69 ± 0.46 | 4.28 ± 0.06 |
| | ID | 81.68 ± 0.38 | 8.11 ± 0.24 | 6.00 ± 0.49 | 4.22 ± 0.09 |
| 4Mo | DC | 83.42 ± 0.66 | 8.20 ± 0.13 | 4.33 ± 0.64 | 4.06 ± 0.13 |
| | ID | 80.99 ± 1.20 | 7.34 ± 0.82 | 7.83 ± 1.01 | 3.84 ± 0.27 |
| 4Hf | DC | 84.82 ± 2.81 | 8.67 ± 1.84 | 5.62 ± 1.01 | 0.88 ± 0.42 |
| | ID | 79.23 ± 0.23 | 10.79 ± 0.62 | 7.48 ± 0.17 | 2.49 ± 0.65 |
| | ID-Eut | 83.14 ± 1.10 | 3.75 ± 1.75 | 3.57 ± 0.51 | 9.55 ± 2.88 |
| 4 W | DC | 82.94 ± 0.43 | 7.63 ± 0.23 | 4.01 ± 0.37 | 5.42 ± 0.34 |
| | ID | 79.57 ± 1.09 | 9.65 ± 0.75 | 9.45 ± 1.25 | 1.34 ± 0.25 |
| 2Re | DC | 84.78 ± 0.48 | 7.91 ± 0.23 | 3.82 ± 0.17 | 3.49 ± 0.21 |
| | ID | 83.31 ± 1.23 | 7.92 ± 0.73 | 8.37 ± 1.60 | 0.40 ± 0.11 |

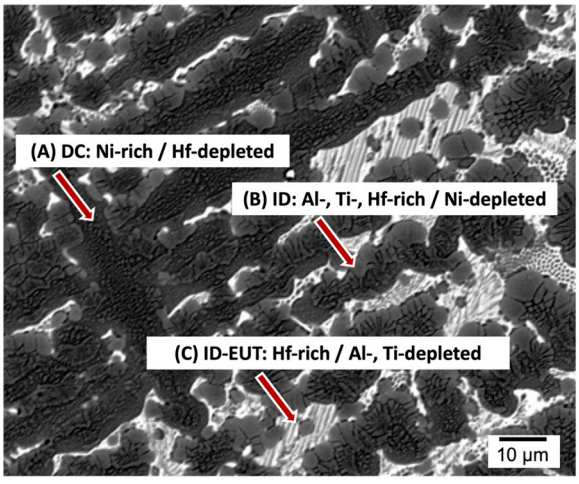


**Fig. 9.** The **4Hf alloy**: Magnified SEM-BSE image of DC-ID region. The as-cast dendritic microstructure comprises three different regions: (A) Dendrite core (DC) Ni-rich and Hf-depleted (dark), (B) inter-dendritic region (ID) Al-, Ti-, Hf-rich and Ni-depleted (grey) and (C) inter-dendritic eutectic region (ID-EUT) Hf-rich and Al-, Ti-depleted (white/grey lamellar).

segregation comparable to that of the as-cast state. The experimental finding contrasts the prediction of our calculation of $\delta_{(t)}$ profiles for Hf in the 4Hf alloy, where sufficient homogenization with $\delta_{(t)} < 20\%$ should be achieved after t < 2 h for diffusion parameter set **Hf 1** (Hf in Ni solid solution, [37]) given in Table 2 and Fig. 4**e**. For diffusion parameter set Hf 2 (Hf in Ni solid solution, [38]) and Hf 3 (Hf in $Ni_3Al$, [38]) our calculation yields $\delta_{(t)} < 20\%$ for $t_{Hf2} < 5$ h and $t_{Hf3} < 7$ h, respectively (Fig. 4**e**), indicating that 1150 °C for t < 7 h may be sufficient for homogenization. In contrast, our 1150 °C / 24 h state still comprises a visible dendritic microstructure with elemental segregation. However, the BSE image generally reveals a less harsh contrast between DC and ID regions (Fig. 8**a-iii**). However, fine very dark, and bright areas are present which we attribute to residual segregation of Al and Ti, and Hf, respectively. The mappings of Al and Ti (Fig. 8**c-iii** and d-**iii**) correlate with the dark ID regions in Fig. 8**a-iii**, while the mapping of Hf (Fig. 8**e-iii**) correlates with the bright ID regions, which we conclude to be residual Hf-rich eutectic.

Sufficient homogenization of the 4Hf alloy could not be achieved due to the presence of eutectic in the ID regions. The low melting point of the eutectic (Fig. 3) limits the maximum temperature for homogenization and thereby increases the required time. The lamellar eutectic phase requires a more complex temperature profile for dissolution and avoiding incipient melting. Although we considered diffusion parameters for diffusion of Hf in Ni solid solution and $Ni_3Al$, our experimental results do not match the predictions based on calculated $\delta_{(t)}$ profiles.

### 3.2.5. *Partitioning coefficient $k'_n$ and residual segregation index $\delta_{(t)}$*

As quantitative measure for homogeneity, the partitioning coefficient $k'_n$ of each element $n$ between DC and ID regions is defined as:

$$k'_n = C_{DC}/C_{ID} \quad (5)$$

with $n$ = Ni, Al, Ti, Cr, Co, Mo, Hf, W or Re; and $C_{DC}$ and $C_{ID}$ are the concentrations in the DC and ID regions, respectively. The calculated values of $k'_n$ using concentrations listed in Table 4 are illustrated in Fig. 10**a**. For all alloys, the partitioning coefficient of Ni is $k'_{Ni} > 1$, with more Ni in the DC region. In the 4Cr, 4Co, 4Ru, 4Mo, 4Hf (DC/ID-Eut) alloys the partitioning coefficient of Al is $k'_{Al} > 1$, and for the 2Re alloy $k'_{Al} = 1$. In contrast, Al in the 4Hf (DC/ID) and 4 W alloy partitions more to the ID region, with $k'_{Al} < 1$. In all alloys, Ti shows a strong tendency to partition to the ID region with $k'_{Ti} < 1$. However, considering the DC and ID-Eut region, Ti partitioning coefficient is inverted with $k'_{Ti} > 1$.

Considering the partitioning behavior of the quaternary additions, we observe three different cases:

i) In the 4Cr, 4Co, 4Ru and 4Mo alloy, X mimics the behavior of Ni, with $k'_X > 1$;
ii) In the 4Hf alloy, X strongly partitions to ID and ID-Eut regions, with $k'_X < 1$;
iii) In the 4W and 2Re alloys, X heavily partitions to ID regions, with $k'_X >> 1$.

In the more complex Ni-based superalloy, Waspalloy, EPMA analysis revealed that Al and Mo were uniformly distributed in DC and ID regions and that segregation was negligible [44], which agrees to our observations for Al for all alloys (except 4Hf), and to that of Mo in the 4Mo alloy. Further resonating with our experimental data, it was also observed that Ti, Cr and Co show significant segregation, with the DC regions being lower in Ti and higher in Cr and Co than interdendritic regions [44].

To predict the time necessary for homogenization of our experimental alloys, we calculated residual segregation index profiles (Fig. 4) using the interdendritic spacing $\lambda$ (Table 1), a homogenization temperature determined by DSC (Fig. 3**a**) and diffusion parameters from the literature (Table 2).

### 3.3. *Microstructure and phase separation behavior after 750 °C / 24 h*

Fig. 11 highlights dark field (DF) transmission electron microscopy (TEM) images. The 4X alloys 4Cr, 4Co, 4Ru, 4Mo and 4 W (Fig. 11**a–e**, respectively) and the 2Re alloy (Fig. 11**f**) are shown after homogenization and aging at 750 °C / 24 h. We note that the 4Hf is omitted here due to its incomplete homogenization (even after 1150 °C / 24 h, see Fig. 8

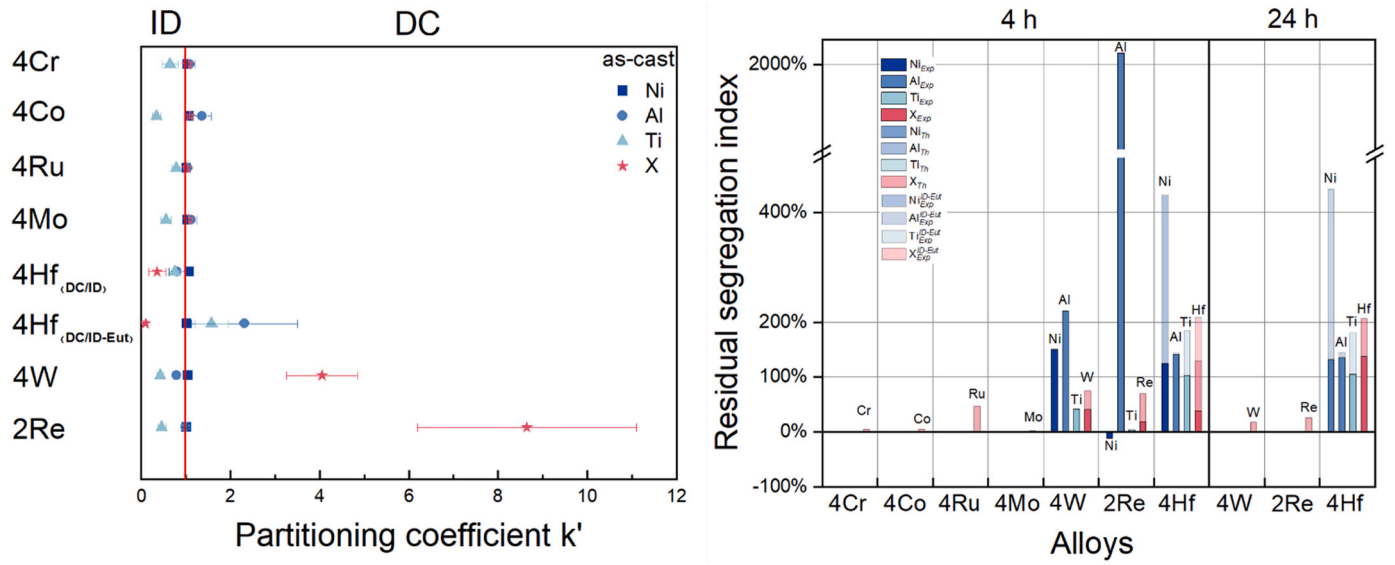


**Fig. 10.** Partitioning coefficients $k'_n$ with n = of Ni, Al, Ti, and Cr, Co, Mo, Ru, Hf, W or Re for the 4Cr, 4Co, 4Ru, 4Mo, 4Hf, 4W and 2Re alloys in the as-cast state. $k'_n$ is calculated using Eq. (5) utilizing the concentration values in Table 4.

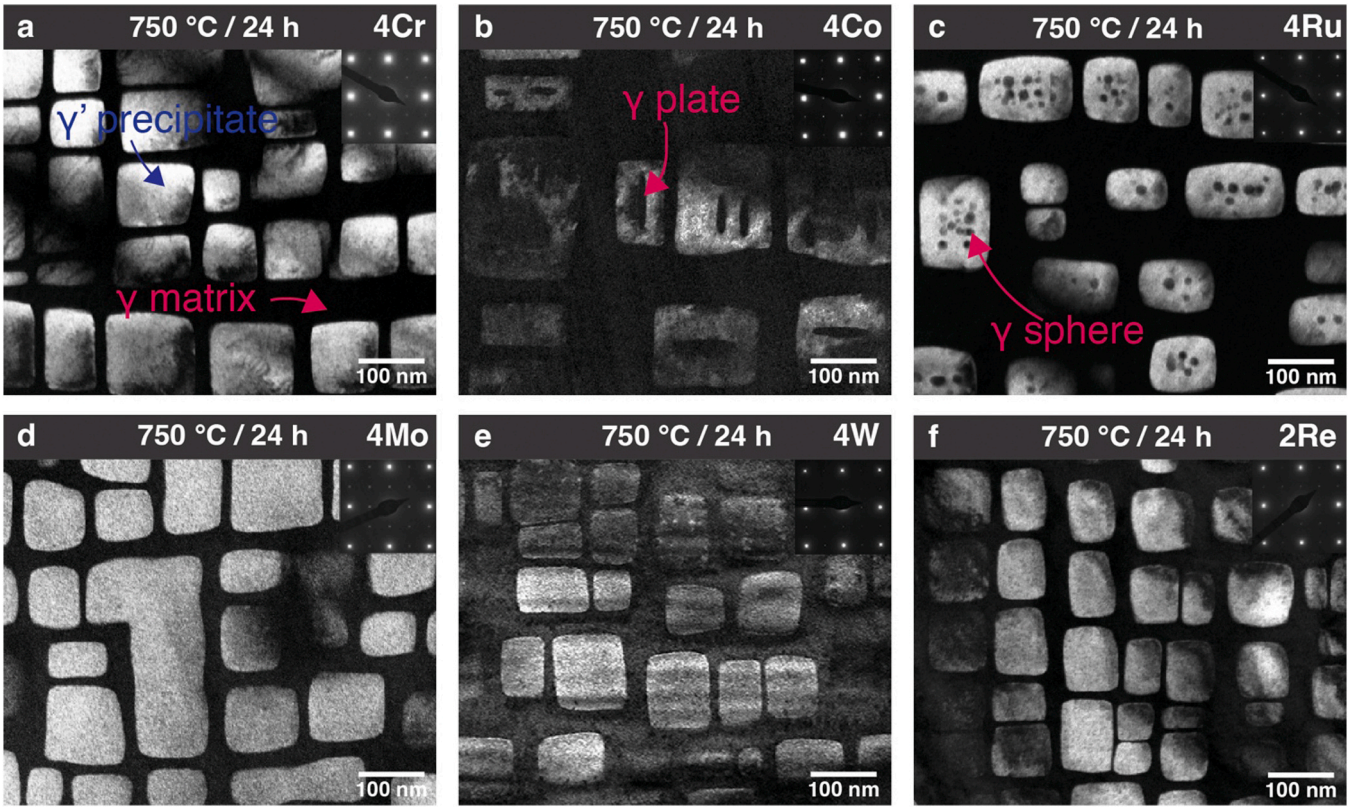


**Fig. 11.** DF-TEM images of 4Cr, 4Co, 4Ru, 4Mo, 4W and 2Re alloys after homogenization and 750 °C / 24 h. Images taken with an $L1_2$ superlattice reflection shown in the SAED in the inset.

and Table 5). Incomplete homogenization leads to locally varying compositions on the micrometer scale, which would bias our investigation of sub-micrometer to nanometer size precipitates and particles. In DF-mode, which is using an $L1_2$ superlattice reflection from the γ' precipitate phase, the γ matrix and particles appear dark while the γ' precipitates appear bright.

Aging at 750 °C / 24 h was chosen as reference condition to ascertain the ability of forming hierarchical microstructures under the influence of quaternary additions of γ forming elements. The ternary base and reference alloy, $Ni_{86.1}Al_{8.5}Ti_{5.4}$ (in at%), and the 750 °C / 24 h condition (among others) has been subject to detailed investigations via transmission electron microscopy (TEM), atom probe tomography (APT), mechanical testing, synchrotron X-ray diffraction (XRD) and finite-element method simulations (FEM), where origin, identity, and formation mechanism of γ particles in hierarchical microstructures, their strengthening effect and lattice parameters were clarified [3,45–48].

**Table 5**
EPMA analysis of 4Cr, 4Co, 4Ru, 4Mo, 4Hf, 4W and 2Re alloys in the homogenized conditions. Concentrations of dendrite core (DC) and interdendritic (ID) regions are given in at%. Errors are standard deviations 2$\sigma$.

| | Homogenized | | | | | | |
|---|---|---|---|---|---|---|---|
| | | | | Concentration, (at%) | | | |
| Alloy | Temperature, (°C) | Time, (h) | Region | Ni | Al | Ti | X |
| 4Cr | 1275 | 4 | 1 | 81.89 ± 0.30 | 8.02 ± 0.26 | 5.82 ± 0.18 | 4.28 ± 0.13 |
| | | | 2 | 82.22 ± 0.27 | 7.94 ± 0.27 | 5.72 ± 0.13 | 4.12 ± 0.11 |
| 4Co | 1275 | 4 | 1 | 81.89 ± 0.21 | 8.17 ± 0.11 | 5.70 ± 0.10 | 4.24 ± 0.08 |
| | | | 2 | 81.89 ± 0.19 | 8.21 ± 0.22 | 5.68 ± .0.17 | 4.22 ± 0.07 |
| 4Ru | 1275 | 4 | 1 | 81.70 ± 0.20 | 8.45 ± 0.14 | 5.89 ± 0.11 | 3.97 ± 0.06 |
| | | | 2 | 81.75 ± 0.14 | 8.36 ± 0.11 | 5.93 ± 0.09 | 3.96 ± 0.07 |
| 4Mo | 1275 | 4 | 1 | 81.92 ± 1.40 | 8.44 ± 1.34 | 5.84 ± 0.68 | 3.81 ± 0.56 |
| | | | 2 | 82.17 ± 0.78 | 8.24 ± 0.82 | 5.64 ± 0.37 | 3.95 ± 0.36 |
| 4 W | 1275 | 4 | DC | 83.16 ± 1.10 | 7.32 ± 0.91 | 5.43 ± 0.41 | 4.09 ± 0.26 |
| | | | ID | 78.08 ± 0.35 | 11.78 ± 0.30 | 7.72 ± 0.29 | 2.42 ± 0.20 |
| | 1275 | 24 | 1 | 82.39 ± 0.46 | 7.98 ± 0.37 | 5.73 ± 0.16 | 3.91 ± 0.09 |
| | | | 2 | 82.40 ± 0.23 | 8.05 ± 0.23 | 5.69 ± 0.07 | 3.86 ± 0.11 |
| 4Hf | 1150 | 4 | DC | 86.17 ± 1.81 | 7.16 ± 0.62 | 5.08 ± 0.59 | 1.58 ± 0.64 |
| | | | ID | 79.19 ± 0.22 | 10.14 ± 0.18 | 6.99 ± 0.12 | 3.68 ± 0.11 |
| | | | ID-Eut | 79.22 ± 1.98 | 0.15 ± 0.56 | 1.43 ± 0.87 | 19.21 ± 3.39 |
| | 1150 | 24 | DC | 86.19 ± 2.01 | 7.31 ± 0.70 | 5.03 ± 0.67 | 1.48 ± 0.69 |
| | | | ID | 79.12 ± 0.60 | 10.19 ± 0.23 | 6.99 ± 0.23 | 3.70 ± 0.26 |
| | | | ID-Eut | 78.91 ± 0.25 | 0.06 ± 0.08 | 1.29 ± 0.10 | 19.74 ± 0.34 |
| 2Re | 1275 | 4 | DC | 84.28 ± 0.37 | 8.07 ± 0.23 | 5.52 ± 0.12 | 2.13 ± 0.21 |
| | | | ID | 84.45 ± 0.24 | 8.33 ± 0.17 | 5.69 ± 0.07 | 1.53 ± 0.20 |
| 2Re | 1275 | 24 | 1 | 84.72 ± 0.23 | 7.95 ± 0.14 | 5.56 ± 0.10 | 1.77 ± 0.13 |
| | | | 2 | 84.77 ± 0.21 | 7.91 ± 0.20 | 5.50 ± 0.07 | 1.82 ± 0.16 |

Hierarchical microstructures in the ternary base alloy after 750 °C / 24 h comprise γ' precipitates with $r_{\gamma'} = 59.5 \pm 14.8$ nm, a volume fraction of $\Phi_{\gamma'} = 30.8 \pm 3.6$ vol% and γ plates with $r_{\gamma p} = 24.1 \pm 9.8$ nm and $\Phi_{\gamma p} = 10 \pm 2$ vol% [3,48]. The area equivalent radii and volume fractions of our experimental alloys and the ternary base alloy listed in Table 6 for comparison. In the quaternary alloys of the present study, Ni of the ternary base alloy was substituted with 4 at% of Cr, Co, Ru, Mo and W or 2 at% Re, as these elements are known to partition to the γ phase, and thus are expected to be enriched in γ matrix as well as γ particles (if present).

Fig. 11**a** shows the 4Cr alloy having a conventional two-phase γ/γ' microstructure, and additional γ particles could not be identified within γ' precipitates. The 4Co alloy (Fig. 11**b**) comprises γ' precipitates that appear larger in size ($r_{\gamma'} \approx 60.3$ nm) and contain γ plates aligned along the elastically soft <001> directions. The addition of 4 at% favors the formation of hierarchical microstructures, comparable to that of the ternary base alloy after the same aging [3]. Compared to the ternary base alloy, γ' precipitates and γ particles appear to have the same morphology but are also larger in size ($r_{\gamma'} \approx 60$ nm and $r_{\gamma p} \approx 16$ nm, respectively). In the 4Ru alloy (Fig. 11**c**), γ' precipitates are present having slightly rounded corners, indicative of Ru's impact on the morphology controlling parameters lattice misfit, elastic properties, and interface energy. Here, we observe a hierarchical microstructure with γ spheres inside γ' precipitates (with sizes of $r_{\gamma'} \approx 48$ nm and $r_{\gamma p} \approx 8$ nm, respectively). γ spheres in γ' precipitates have also been associated with improved strength of the ternary base alloy, after 750 °C / 6 h [3]. The addition of Ru and its slow diffusivity contributes to decelerated growth of γ particles, and thereby to enhanced thermal stability of hierarchical microstructures. Similar γ' precipitates having slightly rounded corners with γ spheres inside were also observed in a $Ni_{83.9}Si_{13}Fe_{3.1}$ alloy (after 650 °C / 24–96 h), where γ spheres showed enhanced morphological stability up to 384 h of aging [49]. In $Ni_{83.9}Si_{13}Fe_{3.1}$ the enhanced microstructural stability of γ spheres was attributed to the dominance of the interfacial energy over the elastic energy that arises from the negative lattice misfit ($\delta \approx -3.3 \times 10^{-3}$) [49]. In contrast, the ternary base alloy, with γ plates, has a positive and relatively large lattice misfit ($\delta \approx 9 \times 10^{-3}$) [48]. The addition of Ru (1.7 at%) to an experimental Ni-based superalloy (containing Al, Ti, Cr, Co, Mo, Ta) with a lattice misfit of $\delta \approx 1 \times 10^{-3}$ was reported to cause a slightly negative lattice misfit close to 0 at room temperature [50]. Hence, we conclude that Ru lowers the lattice parameter in our 4Ru alloy and thereby contributes to the morphological stabilization of γ spheres. A systematic study of the microstructural evolution upon prolonged aging at 750 °C is needed to ascertain the temporal stability of these γ spheres. We conclude that Ru may be an effective candidate for tailoring the stability of hierarchical microstructures in Ni-based superalloys. In the 4Mo, 4W and 2Re alloys (Fig. 11**d–f**), the formation of hierarchical microstructures is not observed after 750 °C / 24 h. As these elements are among the slowest diffusing species in Ni-based superalloys, it may be that γ particles appear only after prolonged aging at 750 °C, beyond 24 h. The size of γ'

**Table 6**
Microstructural parameters of 4Cr, 4Co, 4Ru, 4Mo, 4W and 2Re alloys after homogenization and 750 °C / 24 h. Volume fraction and size of γ' precipitates and γ particles for each alloy are given and compared to the ternary base alloy [3,48]. Not available data is indicated by n.a.

| | | **Aging at 750 °C / 24 h** | | | | | | |
|---|---|---|---|---|---|---|---|---|
| **Phase** | | **4Cr** | **4Co** | **4Ru** | **4Mo** | **4 W** | **2Re** | **Ni-Al-Ti Base**[3,48] |
| **γ' precipitate** | $\Phi_{\gamma'}$, *(vol%)* | 58.5 ± 0.6 | 49.8 ± 5.3 | 36.0 ± 1.5 | 61.1 ± 4.3 | 49.4 ± 2.8 | 47.5 ± 3.9 | 30.8 ± 3.6 |
| | $r_{\gamma'}$, *(nm)* | 58.6 ± 10.8 | 75.8 ± 19.2 | 53.8 ± 10.3 | 55.8 ± 16.5 | 46.7 ± 11.4 | 30.7 ± 11.6 | 59.5 ± 16.9 |
| **γ particle** | $\Phi_{\gamma p}$, *(vol%)* | n.a. | 2.3 ± 0.8 | 2.2 ± 0.2 | n.a. | n.a. | n.a. | 10 ± 2 |
| | $r_{\gamma p}$, *(nm)* | n.a. | 15.9 ± 3.1 | 6.1 ± 1.6 | n.a. | n.a. | n.a. | 24.1 ± 9.8 |

precipitates decreases in the order 4Mo, 4 W and 2Re with $r_{\gamma'} \approx 55$ nm, $r_{\gamma'} \approx 43$ nm and $r_{\gamma'} \approx 31$ nm, respectively (Fig. 11**f**). A summary of size and volume fraction of γ' precipitates and γ particles (if present) for all alloys is highlighted in Table 6.

The ability to form hierarchical microstructures is linked to the supersaturation of γ' precipitates with γ forming elements [3]. The supersaturation of γ' precipitates with Ni and the nanochemical and thermodynamic pathway of formation and evolution of γ particles in γ' precipitates – from Ni-rich clusters to γ spheres, to plates – in the ternary base alloy is well understood [3,45–48]. However, if Ni is substituted with other γ forming, species, the phase separation behavior may completely change. For adding up to 4 at% of Cr, Mo, W (and Hf) and 2 at% of Re, hierarchical microstructures are not formed. We hypothesize two possible pathways for this behavior.

*First,* the addition of up to 4 at% of another γ forming species substantially impacts the supersaturation of γ' precipitates with γ forming elements and/or the solubility of γ forming elements in γ' precipitates, thus lowering the thermodynamic driving force for formation of γ particles.

*Second*, γ' are supersaturated with γ forming elements but the presence of heavier, slow diffusing species significantly slows down diffusion kinetics and thereby formation and growth of such hierarchical particles.

We note that 4 at% represents the upper bound of quaternary additions for which experimental alloys were prepared, and a detailed TEM and APT investigation for additions of X in the range of 0.1–4 at% for different aging times is currently under way. As the influence of quaternary additions of up to 4 at% on homogenization behavior and the ability to form hierarchical microstructures is expected to be the strongest, this series (except 2Re) was chosen for the present study.

## 4. Conclusions

Quaternary additions X of γ forming elements to $Ni_{86.1-n}Al_{8.5}Ti_{5.4}X_n$, Cr, Co, Ru, Mo, Hf, W (n = 4) and Re (n = 2) alter the as-cast dendritic microstructure and thereby the homogenization behavior. For our experimental alloys, the following conclusions on the homogenization behavior can be made:

- The interdendritic distance $\lambda$ varies greatly depending on the quaternary addition with the Cr, Co, Ru and Mo being in the range of 106–120 μm and the Hf, W and Re alloys in the range of 68–81 μm.
- The γ' solvus and the alloys solidus temperatures are similar enough to allow batch homogenization at 1275 °C after which full homogenization could be achieved after 4–24 h (except Hf).
- The Hf alloy required a lower homogenization temperature of 1150 °C and the extensive formation of interdendritic eutectic hindered full homogenization even after 24 h.
- The homogenization behavior could be predicted using experimental data and diffusion parameters to model the residual segregation index $\delta$ (except Hf).

The influence of quaternary additions on the formation of hierarchical microstructures and the morphology of γ particles allows the following conclusions:

- Hierarchical microstructures were not observed for the Cr, Mo, Hf, W and Re alloys, which indicates either that longer aging at 750 °C is required as diffusion kinetics are dramatically slowed down, or that the additional element and its amount alter the ability of γ' precipitates to become supersaturated with γ forming elements and subsequently form of γ particles.
- Hierarchical microstructures formed in the Co (γ plates) and Ru (γ spheres) alloys.
- The spherical morphology of γ particles suggests Ru to be an effective candidate to tailor the phase stability of hierarchical γ particles and thereby improve the stability of hierarchical microstructures.

## CRediT authorship contribution statement

**Y. Ma:** Software, Formal analysis, Visualization, Writing original draft. **M. Huang:** Investigation, Formal analysis, Visualization, Writing original draft. **Y. Wu:** Formal analysis, resources, Writing – review & editing. **W. Zheng:** Formal analysis, resources, Writing – review & editing. **M.J. Pavel:** Software, Formal analysis, Visualization, Writing – review & editing. **M.L. Weaver:** Software, Resources, Writing – review & editing. **W. Meng:** Investigation, Formal analysis, Visualization. **Y. Long:** Investigation, resources, Writing – review & editing. **S. Ngai:** Conceptualization, Supervision, Resources, Writing – review & editing. **X.J. Wang:** Methodology, Investigation, Supervision, Writing – review & editing. **P. Zhang:** Investigation, Visualization, Writing – review & editing. **W. Li:** Methodology, Investigation, Supervision, Writing – review & editing. **F. Vogel:** Conceptualization, Methodology, Investigation, Supervision, Writing – review & editing.

## Declaration of Competing Interest

The authors declare that they have no known competing financial interests or personal relationships that could have appeared to influence the work reported in this paper.

## Data Availability

Data will be made available on request.

## Acknowledgements

F.V. acknowledges financial support by the National Natural Science Foundation of China (NSFC grant No. 52150610488), the National Natural Science Foundation of Guangdong, China (grant No. 2021A1515010563), the University of Science and Technology Beijing, State Key Lab of Advanced Metals and Materials (grant No. 2021-ZD09), the South China University of Technology, National Engineering Research Center of Near-Net-Shape Forming for Metallic Materials Open Fund, China (grant No. 2020001). M.J.P. and M.L.W. were partially supported by the National Science Foundation, US (DMR-2105364). This work was supported by Nova Scientific (Guangzhou) Co., Ltd. (www.novascitech.com), Lin Chen and Valerie Du are gratefully acknowledged for their help with TEM sample preparation and TEM imaging.

## References

[1] J. Wu, X. Jiang, Y. Wang, J. Dong, L. Lou, Effects of Ta on microstructural stability and mechanical properties of hot corrosion resistant Ni-based single crystal superalloys during long-term thermal exposure, Mater. Sci. Eng.: A 806 (2021), 140829, https://doi.org/10.1016/j.msea.2021.140829.
[2] Y.S. Fan, X.G. Yang, D.Q. Shi, L. Tan, W.Q. Huang, Quantitative mapping of service process-microstructural degradation-property deterioration for a Ni-based superalloy based on chord length distribution imaging process, Mater. Des. 203 (2021), 109561, https://doi.org/10.1016/j.matdes.2021.109561.
[3] F. Vogel, N. Wanderka, Z. Balogh, M. Ibrahim, P. Stender, G. Schmitz, J. Banhart, Mapping the evolution of hierarchical microstructures in a Ni-based superalloy, Nat. Commun. 4 (1) (2013) 7, https://doi.org/10.1038/ncomms3955.
[4] G. Song, Z. Sun, L. Li, X. Xu, M. Rawlings, C.H. Liebscher, B. Clausen, J. Poplawsky, D.N. Leonard, S. Huang, Z. Teng, C.T. Liu, M.D. Asta, Y. Gao, D.C. Dunand, G. Ghosh, M. Chen, M.E. Fine, P.K. Liaw, Ferritic alloys with extreme creep resistance via coherent hierarchical precipitates, Sci. Rep. 5 (2015), 16327, https://doi.org/10.1038/srep16327.
[5] G. Song, Z. Sun, J.D. Poplawsky, Y. Gao, P.K. Liaw, Microstructural evolution of single Ni2TiAl or hierarchical NiAl/Ni2TiAl precipitates in Fe-Ni-Al-Cr-Ti ferritic alloys during thermal treatment for elevated-temperature applications, Acta Mater. 127 (2017) 1–16, https://doi.org/10.1016/j.actamat.2017.01.011.

[6] Gian Song, Microstructure and Creep Deformation Behavior of a Hierarchical-Precipitate-Strengthened Ferritic Alloy with Extreme Creep Resistance (PhD Dissertation), University of Tennessee, 2016.

[7] S. Antonov, D. Isheim, D.N. Seidman, E. Sun, R.C. Helmink, S. Tin, γ′ phase instabilities in high refractory content γ-γ′ In-base superalloys, Proc. Int. Symp. Superalloys (2016) 199–208, https://doi.org/10.1002/9781119075646.ch22.

[8] Y.-T. Chen, Y.-J. Chang, H. Murakami, T. Sasaki, K. Hono, C.-W. Li, K. Kakehi, J.-W. Yeh, A.-C. Yeh, Hierarchical microstructure strengthening in a single crystal high entropy superalloy, Sci. Rep. 10 (2020), 12163, https://doi.org/10.1038/s41598-020-69257-8.

[9] S. Meher, L.K. Aagesen, M.C. Carroll, T.M. Pollock, L.J. Carroll, The origin and stability of nanostructural hierarchy in crystalline solids, Sci. Adv. 4 (2018), eaao6051, https://doi.org/10.1126/sciadv.aao6051.

[10] Q. Ding, H. Bei, X. Zhao, Y. Gao, Z. Zhang, Processing, microstructures and mechanical properties of a Ni-based single crystal superalloy, Crystals 10 (2020) 1–14, https://doi.org/10.3390/cryst10070572.

[11] Y.G. Tan, F. Liu, A.W. Zhang, D.W. Han, X.Y. Yao, W.W. Zhang, W.R. Sun, Element segregation and solidification behavior of a Nb, Ti, Al Co-strengthened superalloy ЭК151, Acta Metall. Sin. (Engl. Lett. ) 32 (2019) 1298–1308, https://doi.org/10.1007/s40195-019-00894-3.

[12] J.O. Andersson, T. Helander, L.H. Hoglund, P.F. Shi, B. Sundman, Thermo-Calc & DICTRA, computational tools for materials science, Calphad 26 (2002) 273–312.

[13] ThermoCalc Software, TCNi12: TCS Ni-based Superalloys Database, (2021). ⟨https://thermocalc.com/products/databases/nickel-based-alloys/⟩.

[14] R.M. Kearsey, J.C. Beddoes, P. Jones, P. Au, Compositional design considerations for microsegregation in single crystal superalloy systems, Intermet. (Barking) (2004) 903–910, https://doi.org/10.1016/j.intermet.2004.02.041.

[15] S.R. Hegde, R.M. Kearsey, J. Beddoes, Design of Solutionizing Heat Treatments for an Experimental Single Crystal Superalloys, 2008.

[16] P. Hallensleben, H. Schaar, P. Thome, N. Jöns, A. Jafarizadeh, I. Steinbach, G. Eggeler, J. Frenzel, On the evolution of cast microstructures during processing of single crystal Ni-base superalloys using a Bridgman seed technique, Mater. Des. 128 (2017) 98–111, https://doi.org/10.1016/j.matdes.2017.05.001.

[17] O.M. Horst, D. Adler, P. Git, H. Wang, G. Eggeler, Exploring the fundamentals of Ni-based Superalloy single crystal (SX) alloy design: chemical composition vs. microstructure, Mater. Des. 195 (2020), 108976.

[18] N. Ren, J. Li, B. Wang, L. Zeng, M. Xia, J. Li, Design of variable withdrawal rate for superalloy single-crystal blade fabrication, Mater. Des. 198 (2021), 109347, https://doi.org/10.1016/j.matdes.2020.109347.

[19] W. Xu, F. Wang, D. Ma, X. Zhu, D. Li, A. Bührig-Polaczek, Sliver defect formation in single crystal Ni-based superalloy castings, Mater. Des. 196 (2020), 109138, https://doi.org/10.1016/j.matdes.2020.109138.

[20] B. Ruttert, M. Ramsperger, L. Mujica Roncery, I. Lopez-Galilea, C. Körner, W. Theisen, Impact of hot isostatic pressing on microstructures of CMSX-4 Ni-base superalloy fabricated by selective electron beam melting, Mater. Des. 110 (2016) 720–727, https://doi.org/10.1016/j.matdes.2016.08.041.

[21] C. Stewart, S. Murray, A. Suzuki, T. Pollock, C. Levi, Accelerated discovery of oxidation resistant CoNi-base γ/γ' alloys with high L12 solvus and low density, Mater. Des. 189 (2020), 108445, https://doi.org/10.1016/j.matdes.2019.108445.

[22] S.R. Hegde, R.M. Kearsey, J.C. Beddoes, Designing homogenization-solution heat treatments for single crystal superalloys, Mater. Sci. Eng. A 527 (2010) 5528–5538, https://doi.org/10.1016/j.msea.2010.05.019.

[23] R.M. Kearsey, J.C. Beddoes, P. Jones, P. Au, Compositional design considerations for microsegregation in single crystal superalloy systems, Intermet. (Barking) 12 (2004) 903–910, https://doi.org/10.1016/j.intermet.2004.02.041.

[24] R.M. Kearsey, J.C. Beddoes, K.M. Jaansalu, W.T. Thompson, P. Au, The effects of Re, W and Ru on microsegregation behaviour in single crystal superalloy systems, Proc. Int. Symp. . Superalloys (2004) 801–810, https://doi.org/10.7449/2004/superalloys_2004_801_810.

[25] M.M.P. Janssen, Diffusion in the Nickel-Rich Part of the Ni-AI System at 1000 ℃ to 1300 ℃ Ni3AI Layer Growth, Diffusion Coefficients, and Interface Concentrations, n.d.

[26] M.S.A. Karunaratne, P. Carter, R.C. Reed, ON THE DIFFUSION OF ALUMINIUM AND TITANIUM IN THE Ni-RICH Ni-Al-Ti SYSTEM BETWEEN 900 AND 1200°C, 2001. www.elsevier.com.

[27] T. Gheno, F. Jomard, C. Desgranges, L. Martinelli, Tracer diffusion of Cr in Ni and Ni-22Cr studied by SIMS, Mater. (Oxf. ) 3 (2018) 145–152, https://doi.org/10.1016/j.mtla.2018.08.004.

[28] S.B. Jung, T. Yamane, K. Hirao, H. Araki, S. Saji, Interdiffusion and its size effect in nickel solid solutions of Ni-Co, Ni-Cr and Ni-Ti systems, 1992.

[29] D. Pruthi, M. Anand, R. Agarwala, Diffusion of chromium in inconemoo, J. Nucl. Mater. 64 (1977) 206–210.

[30] A.B. Vladimirov, V.N. Kajgorodov, S.M. Klotsman, I. Sh, Trakhtenberg, Volume diffusion of cobalt and tungsten in nickel, Fiz. Met. i Metalloved. 46 (1978) 1232–1239.

[31] Q. Wu, S.S. Li, Y. Ma, S.K. Gong, First principles calculations of alloying element diffusion coefficients in Ni using the five-frequency model, Chin. Phys. B 21 (2012), 109102, https://doi.org/10.1088/1674-1056/21/10/109102.

[32] M.S.A. Karunaratne, R.C. Reed, Interdiffusion of the platinum-group metals in nickel at elevated temperatures, Acta Mater. 51 (2003) 2905–2919, https://doi.org/10.1016/S1359-6454(03)00105-8.

[33] E. Mabruri, S. Sakurai, Y. Murata, T. Koyama, M. Morinaga, Interdiffusion in Ni-Co-Re and Ni-Co-Ru systems, Mater. Trans. 48 (2007) 2718–2723, https://doi.org/10.2320/matertrans.MRA2007116.

[34] M.S.A. Karunaratne, R.C. Reed, Interdiffusion of niobium and molybdenum in nickel between 900–1300 °C, in: Defect and Diffusion Forum, Trans Tech Publications Ltd, 2005, pp. 420–425, https://doi.org/10.4028/www.scientific.net/ddf.237-240.420.

[35] C.P. Heijwegen, G.D. Rieck, Determination of the phase diagram of the molybdenum-nickel system using diffusion couples and equilibrated alloys, Int. J. Mater. Res. 64 (1973) 450–453, https://doi.org/10.1515/ijmr-1973-640608.

[36] Y.E. Ugaste, Mutual diffusion in nickel-molybdenum and palladium-molybdenum alloys, Fiz. Metal. Metalloved. 33 (1972) 1034–1039.

[37] D. Bergner, Zur Diffusion von Hf und Ti in Ni, Krist. Und Tech. 7 (1972) 651–656.

[38] S. Ma, Y. Zheng, Diffusion behaviour of Hf in Ni and Ni3Al, Chin. J. Mater. Res. 10 (1996) 149–152.

[39] J.M. Walsh, M.J. Donachie, S.M.E. Met, A.D.I.M. Sc, Interdiffusion in the nickel-tungsten and thoria-dispersed nickel-tungsten systems, Met. Sci. J. 3 (1969) 68–74.

[40] M. Karunaratne, P. Carter, R. Reed, Interdiffusion in the face-centred cubic phase of the Ni-Re, Ni-Ta and Ni-W systems between 900 and 1300°C, 2000. www.elsevier.com/locate/msea.

[41] C.E. Campbell, W.J. Boettinger, U.R. Kattner, Development of a diffusion mobility database for Ni-base superalloys, Acta Mater. 50 (2002) 775–792.

[42] Q.N. Fan, C.Y. Wang, T. Yu, J.P. Du, A ternary Ni-Al-W EAM potential for Ni-based single crystal superalloys, Phys. B Condens Matter 456 (2015) 283–292, https://doi.org/10.1016/j.physb.2014.09.012.

[43] E. Mabruri, M. Hattori, K. Hasuike, T. Kunieda, Y. Murata, M. Morinaga, Al and Re interdiffusion in the γ-phase of Ni-Al-Re system, Mater. Trans. (2006) 1408–1411, https://doi.org/10.2320/matertrans.47.1408.

[44] S.L.L. Semiatin, R.C. Kramb, R.E. Turner, F. Zhang, M.M. Antony, Analysis of the homogenization of a nickel-base superalloy, Scr. Mater. 51 (2004) 491–495, https://doi.org/10.1016/j.scriptamat.2004.05.049.

[45] F. Vogel, N. Wanderka, S. Matsumura, J. Banhart, Early stages of decomposition within the γ′ phase of a Ni–Al–Ti model alloy, Intermet. (Barking) 22 (2012) 226–230, https://doi.org/10.1016/j.intermet.2011.11.011.

[46] F. Vogel, N. Wanderka, Z. Balogh, M. Ibrahim, P. Stender, G. Schmitz, T. Fedorova, J. Banhart, Evolution of nanoscale clusters in γ′ precipitates of a Ni–Al–Ti model alloy, Ultramicroscopy 159 (2015) 1–7, https://doi.org/10.1016/j.ultramic.2015.04.021.

[47] F. Vogel, S. Ngai, K. Fricke, M. McKechnie, N. Wanderka, T. Hentrich, J. Banhart, G.B. Thompson, Tracing the three-dimensional nanochemistry of phase separation in an inverse Ni-based superalloy, Acta Mater. 157 (2018) 326–338, https://doi.org/10.1016/j.actamat.2018.07.038.

[48] F. Vogel, J. Cheng, S.B. Liang, C.B. Ke, S.S. Cao, X.P. Zhang, I. Zizak, A.M. Manzoni, J.M. Yu, N. Wanderka, W. Li, Formation and evolution of hierarchical microstructures in a Ni-based superalloy investigated by in situ high-temperature synchrotron X-ray diffraction, J. Alloy. Compd. 919 (2022), 165845, https://doi.org/10.1016/j.jallcom.2022.165845.

[49] E. Zaiser, X.Y. Zhou, A.M. Manzoni, S. Haas, U. Glatzel, X.P. Zhang, G. B. Thompson, W. Li, F. Vogel, Hierarchical phase separation behavior in a Ni-Si-Fe alloy, Acta Mater. 195 (2020) 1–14, https://doi.org/10.1016/j.actamat.2020.05.023.

[50] S. Neumeier, F. Pyczak, M. Göken, Influence of rhenium and ruthenium on the local mechanical properties of the γ and γ′ phases in nickel-base superalloys, Philos. Mag. 91 (2011) 4187–4199.